Stress and deformation mechanisms at a subduction zone: insights from 2D thermo-mechanical numerical modelling

Annelore Bessat[1], Thibault Duretz[2,1], György Hetényi[1], Sébastien Pilet[1] and Stefan M. Schmalholz[1]

[1] Institute of Earth Sciences, University of Lausanne, 1015 Lausanne, Switzerland

[2] Univ Rennes, CNRS, Géosciences Rennes – UMR 6118, F-35000 Rennes, France

annelore.bessat@unil.ch

submitted to Geophysical Journal International

Section: Geodynamics and tectonics

Abbreviated title: Stress and deformation mechanisms at subduction zones

This article has been accepted for publication in Geophysical Journal International ©: 2020 Bessat, A., Duretz, T., Hetényi, G., Pilet, S., and Schmalholz, S.M. *Published by Oxford University Press on behalf of the Royal Astronomical Society. All rights reserved.*

This is an authors' pre-print version of this paper. The final version is available here: https://academic.oup.com/gji/advance-article-abstract/doi/10.1093/gji/ggaa092/5743420 or via the DOI https://doi.org/10.1093/gji/ggaa092

Summary

Numerous processes such as metamorphic reactions, fluid and melt transfer and earthquakes occur at a subducting zone, but are still incompletely understood. These processes are affected, or even controlled, by the magnitude and distribution of stress and deformation mechanism. To eventually understand subduction zone processes, we quantify here stresses and deformation mechanisms in and around a subducting lithosphere, surrounded by asthenosphere and overlain by an overriding plate.

We use two-dimensional thermo-mechanical numerical simulations based on the finite difference and marker-in-cell method and consider a 3200 km wide and 660 km deep numerical domain with a resolution of 1 km by 1 km. We apply a combined visco-elasto-plastic deformation behaviour using a linear combination of diffusion creep, dislocation creep and Peierls creep for the viscous deformation. We consider two end-member subduction scenarios: forced and free subduction. In the forced scenario, horizontal velocities are applied to the lateral boundaries of the plates during the entire simulation. In the free scenario, we set the horizontal boundary velocities to zero once the subducted slab is long enough to generate a slab pull force large enough to maintain subduction without horizontal boundary velocities. A slab pull of at least 1.8 TN m^{-1} is required to continue subduction in the free scenario. We also quantify along-profile variations of gravitational potential energy (GPE). We evaluate the contributions of topography and density variations to GPE variations across a subduction system. The GPE variations indicate large-scale horizontal compressive forces around the trench region and extension forces on both sides of the trench region. Corresponding vertically-averaged differential stresses are between 120 and 170 MPa. Furthermore, we calculate the distribution of the dominant deformation mechanisms. Elasto-plastic deformation is the dominant mechanism in the upper region of the lithosphere and subducting slab (from ca. 5 to 60 km depth from the top of the slab). Viscous deformation dominates in the lower region of the lithosphere and in the asthenosphere. Considering elasticity in the calculations has an important impact on the magnitude and distribution of deviatoric stress; hence, simulations with increased shear modulus, in order to reduce elasticity, exhibit considerably different stress fields. Limiting absolute stress magnitudes by decreasing the internal friction angle causes slab detachment so that slab pull cannot be transmitted anymore to the horizontal lithosphere. Applying different boundary conditions shows that forced subduction simulations are stronger affected by the applied boundary conditions than free subduction simulations. We also compare our modelled topography and gravity anomaly with natural data of seafloor bathymetry and free-air gravity anomalies across the Mariana trench. Elasticity and deviatoric

stress magnitudes of several hundreds of MPa are required to best fit the natural data. This agreement suggests that the modelled flexural behaviour and density field are compatible with natural data. Moreover, we discuss potential applications of our results to the depth of faulting in a subducting plate and to the generation of petit-spot volcanoes.

Keywords :

Numerical modelling; Subduction zone processes; Lithospheric flexure; Rheology: mantle; Dynamics: gravity and tectonics

1. - Introduction

Subduction zones are critical locations on Earth where the oceanic lithosphere dives into the convecting mantle and, hence, contributes to the cooling of the Earth and to the recycling of rocks and water (e.g. Stern, 2002; Turcotte & Schubert, 2014; Crameri et al., 2019). Many geophysical and geochemical processes are related to subduction zones, such as hydration of the mantle wedge and associated melt generation related to arc magmatism (e.g. Plümper et al., 2016), major earthquakes observed at different depths in the subducting slab and at megathrusts (e.g. Youngs et al., 1997), water transport in subducting slabs along faults (e.g. Faccenda et al., 2009) or the generation of petit-spot volcanoes, which might be associated with plate flexure around subduction zones (Hirano et al., 2006; Yamamoto et al., 2014). However, many of these processes are still incompletely understood. Processes inside and around subducting plates are, to a larger or smaller extent, controlled by the magnitude and the type of stress (extensive, compressive or shear) and by the dominant deformation mechanism (elastic, frictional-plastic or viscous). Since it is not possible to study stress and deformation mechanisms around subduction zones *in situ*, indirect approaches like geophysical imaging (e.g. Kearey et al., 2009) and numerical modelling in two-dimensions (2D) (e.g. Gurnis et al., 2004; Yamato et al., 2007; Schmeling et al., 2008; Gerya, 2011) and 3D (e.g. Schellart et al., 2007; Yamato et al., 2009;

74 Duretz et al., 2014) are frequently used to study subduction systems. Numerical models are suitable
75 to quantify the magnitude of stress and the associated distribution of deformation mechanisms for
76 subduction systems (e.g. Čížková et al., 2007; Garel et al., 2014). A better understanding of the
77 magnitude of stress, their distribution and their associated dominant deformation mechanisms in
78 subduction systems might ultimately help us to understand subduction-related geophysical and
79 geochemical processes.
80 The main aim of this study is to quantify stresses and to determine the distribution of stress and
81 dominant deformation mechanism around flexural regions in a subducting plate. Although there are
82 numerous studies of numerical subduction simulations, only few numerical models quantified the
83 distribution of stress (e.g. Hassani et al., 1997; Funiciello et al., 2003; Sobolev et al., 2006; Čížková et
84 al., 2007; Babeyko & Sobolev, 2008; Farrington et al., 2014; Holt et al., 2015) and deformation
85 mechanisms (e.g. Čížková et al., 2007; Garel et al., 2014). Like all models, they have limitations in their
86 hypotheses, such as neglecting elastic deformation (e.g. Čížková et al., 2007; Chertova et al., 2012;
87 Garel et al., 2014; Holt et al., 2015), no or only one creep deformation mechanism (e.g. Hassani et al.,
88 1997; Funiciello et al., 2003; Farrington et al., 2014), a prescribed slab geometry (e.g. Sobolev et al.,
89 2006; Babeyko & Sobolev, 2008), no free surface boundary condition (e.g. Čížková et al., 2007; Holt et
90 al., 2015) or a yield stress being a function of depth only (e.g. Čížková et al., 2007; Garel et al., 2014)
91 and not a function of the total pressure (negative mean stress). Here, we build on the above mentioned
92 models, but without the mentioned limitations with the aim to make a step further in calculating stress
93 and dominant deformation mechanisms at subduction systems. We apply a high-resolution (1 km grid
94 spacing) 2D thermo-mechanical numerical model of the lithosphere-asthenosphere system and we
95 consider five deformation mechanisms: elastic, frictional-plastic (Mohr-Coulomb criterion), diffusion
96 creep, dislocation creep and Peierls creep. We apply a local iteration strategy to correctly calculate the
97 partitioning of the strain rate between these five deformation mechanisms, because calculations
98 without such iterations overestimate the calculated stress (Schmalholz & Duretz, 2017). Furthermore,

we consider two subduction scenarios, which represent two end-member conditions with respect to the forces driving subduction: (1) forced subduction whereby the subducting plate is pushed by far-field horizontal velocity (e.g., by ridge push), and (2) free subduction whereby subduction is driven only by the negative buoyancy of the subducting plate itself (slab pull). We initiate free subduction by forced subduction but set the far-field velocity to zero once slab pull is large enough to drive free subduction. We quantify the required minimum slab pull force to drive free subduction for our model configuration. We also quantify along-profile variations of gravitational potential energy (e.g., Molnar & Lyon-Caen, 1988; Molnar et al., 1993; Schmalholz et al., 2014; Schmalholz et al., 2019) across the subduction system, because these GPE variations cause horizontal forces and, hence, stresses. We also investigate whether differentiating criteria between forced and free subduction exist and what these criteria are. Furthermore, we evaluate the impact of elasticity and yield stress on the deformation and stress field around subduction zones. We do not configure our model to fit a particular subduction system, but in order to evaluate whether the modelled subductions are applicable to natural subduction zones, we finally compare the modelled topography and gravity anomalies with natural data from the Mariana subduction zone, which is a type-example for an ocean-ocean subduction system and has often been used for comparison with theoretical models (e.g., Funiciello et al., 2003; Turcotte & Schubert, 2014).

2. - Mathematical model

2.1 Governing equations for numerical simulations

We use the 2D thermo-mechanical code MDoodz, which is based on the finite difference and marker-in-cell method (e.g. Duretz et al. 2011b; Gerya, 2019). The steady-state force balance equation is

$$\frac{\partial \sigma_{ij}}{\partial x_j} + \rho g_i = 0 \qquad (1)$$

where i and j run from 1 to 2, 1 indicates horizontal and 2 vertical dimension, σ_{ij} are the components of the total stress tensor, x_j represents the spatial coordinates, ρ is the density and $g_i = [0, -g]$ is the gravitational acceleration vector with *g* being the gravitational acceleration. The conservation of mass for incompressible material is

$$\frac{\partial v_i}{\partial x_i} = 0 \tag{2}$$

where v_i are the components of the velocity vector. The temperature evolution equation is

$$\rho c \frac{\mathrm{d}T}{\mathrm{d}t} = \frac{\partial}{\partial x_i}\left(k \frac{\partial T}{\partial x_i}\right) + H_D + H_R \tag{3}$$

where d*/*d*t* represents the total time derivative, *c* the specific heat, *k* the thermal conductivity, H_R the radiogenic heat production and H_D the heating due to viscous and plastic dissipative work (here we assume that all dissipative work is converted into heat, i.e., Taylor-Quinney coefficient is 1, since we do not model grain size reduction).

The density is calculated with the following equation of state:

$$\rho = \rho_0[1 + \beta(P - P_0)] * [1 - \alpha(T - T_0)] \tag{4}$$

where ρ_0 is the reference density at a reference pressure P_0 and temperature T_0, P is the pressure (negative mean stress), T is the temperature, α is the thermal expansion and β is the compressibility. The components of the total stress tensor are

$$\sigma_{ij} = -P\delta_{ij} + \tau_{ij} \tag{5}$$

where δ_{ij} is the Kronecker delta ($\delta_{ij} = 1$ when $i = j$ and $\delta_{ij} = 0$ when $i \neq j$) and τ_{ij} are the components of the deviatoric stress tensor. We consider a visco-elasto-plastic rheology described by a Maxwell model (Moresi et al., 2003; Popov & Sobolev, 2008):

$$\dot{\varepsilon}_{ij} = \dot{\varepsilon}_{ij}^{\mathrm{vis}} + \dot{\varepsilon}_{ij}^{\mathrm{el}} + \dot{\varepsilon}_{ij}^{pl} = \frac{1}{2\eta}\tau_{ij} + \frac{1}{2G}\frac{D\tau_{ij}}{Dt} + \dot{\gamma}\frac{\partial Q}{\partial \tau_{ij}} \tag{6}$$

where superscripts $\dot{\varepsilon}_{ij}^{\mathrm{vis}}$, $\dot{\varepsilon}_{ij}^{\mathrm{el}}$ and $\dot{\varepsilon}_{ij}^{\mathrm{pl}}$ indicate viscous, elastic and plastic deviatoric strain rate tensors, respectively. The quantity η represents the effective viscosity, G is the shear modulus, t is the time,

139 D/Dt indicates the objective time derivative (e.g., Schmalholz et al., 2001), Q is the plastic flow
140 potential and $\dot{\gamma}$ is a plastic multiplier rate.

141 Frictional-plastic yielding is described by a Drucker-Prager criterion with the yield stress, τ_{yield}

$$\tau_{\mathrm{yield}} = C\cos(\Theta) + P\sin(\Theta) \tag{7}$$

142 where C is the cohesion and Θ is the angle of internal friction. The yield function, *F*, is expressed as
143 $F = \tau_{\mathrm{II}} - \tau_{\mathrm{yield}}$ and the plastic potential is formulated as $Q = \tau_{\mathrm{II}}$, being the square root of the
144 second invariant of the deviatoric stress tensor. Plastic deformation occurs whenever $F \geq 0$. The
145 plastic multiplier rate is computed as $\dot{\gamma} = 2\dot{\varepsilon}_{II} - \frac{\tau_{\mathrm{yield}} - {\tau_{\mathrm{II}}}^{\mathrm{old}}}{G\mathrm{d}t} + \frac{\tau_{\mathrm{yield}}}{\eta}$ or simply $\dot{\gamma} = \frac{F}{\eta^{\mathrm{ve}}}$, where $\eta^{\mathrm{ve}} =$
146 $\left(\frac{1}{\eta} + \frac{1}{G\mathrm{d}t}\right)^{-1}$, ${\tau_{ij}}^{\mathrm{old}}$ are advected and rotated stress components from the previous time step and $\mathrm{d}t$
147 is the time step. Subsequently, the plastic strain rate tensor is evaluated as $\dot{\varepsilon}_{ij}^{\mathrm{pl}} = \dot{\gamma}\frac{\partial Q}{\partial \tau_{ij}} = \dot{\gamma}\frac{\tau_{ij}}{2\tau_{\mathrm{II}}}$. In
148 practice, the stress state is mapped back onto the yield surface by modifying the effective viscosity as:

$$\eta = \eta^{\mathrm{pl}} = \frac{\tau_{\mathrm{yield}}}{2\dot{\varepsilon}_{\mathrm{II}}^{\mathrm{eff}}} \tag{8}$$

149

150 where $\dot{\varepsilon}_{\mathrm{II}}^{\mathrm{eff}}$ is the square root of the second invariant of the effective strain rate tensor, defined as

$$\dot{\varepsilon}_{ij}^{\mathrm{eff}} = \dot{\varepsilon}_{ij} + \frac{{\tau_{ij}}^{\mathrm{old}}}{2G\mathrm{d}t} \tag{9}$$

151 The viscous deformation is a linear combination of flow laws for diffusion creep (Hirth & Kohlstedt,
152 2003), dislocation creep (Hirth & Kohlstedt, 2003) and Peierls creep (Kameyama et al., 1999):

$$\dot{\varepsilon}_{ij}^{\mathrm{vis}} = \dot{\varepsilon}_{ij}^{\mathrm{dif}} + \dot{\varepsilon}_{ij}^{\mathrm{dis}} + \dot{\varepsilon}_{ij}^{\mathrm{pei}} \tag{10}$$

153

154 Diffusion creep (i.e., linear creep) is given by

$$\dot{\varepsilon}_{ij}^{\mathrm{dif}} = F_{\mathrm{dif}} A_{\mathrm{dif}} {\tau_{ij}}^{n_{\mathrm{dif}}} d^{-m_{\mathrm{dif}}} \exp\left(-\frac{E_{\mathrm{dif}}^{*} + PV_{\mathrm{dif}}^{*}}{RT}\right) \tag{11}$$

155 Dislocation creep (i.e., power law creep) is given by

$$\dot{\varepsilon}_{ij}^{\mathrm{dis}} = F_{\mathrm{dis}} A_{\mathrm{dis}} \tau_{ij}^{n_{\mathrm{dis}}} d^{-m_{\mathrm{dis}}} \exp\left(-\frac{E_{\mathrm{dis}}^{*} + PV_{\mathrm{dis}}^{*}}{RT}\right) \quad (12)$$

156 Peierls creep (i.e., low-temperature plasticity or exponential creep) is given by

$$\dot{\varepsilon}_{ij}^{\mathrm{pei}} = F_{\mathrm{pei}} A_{\mathrm{pei}} \exp\left[-\frac{E_{\mathrm{pei}}}{RT}(1-\gamma)^{n_{\mathrm{pei}}}\right]\left(\frac{\tau_{ij}}{\gamma\sigma_{\mathrm{pei}}}\right)^{S} \quad (13)$$

157 with

$$S = \frac{E_{\mathrm{pei}}}{RT}(1-\gamma)^{(n_{\mathrm{pei}}-1)} n_{\mathrm{pei}}\gamma \quad (14)$$

158 In the above flow laws, F is a transformation factor to transform flow laws fitted form rock
159 deformation data to flow laws for tensor components (e.g., Schmalholz & Fletcher, 2011; Gerya, 2019),
160 A is a material constant determined from laboratory measurements, n is the stress exponent, d is the
161 grain size, m is the grain size exponent, E is the activation energy, V is the activation volume, R is the
162 gas constant, γ is an adjustable constant (Kameyama et al., 1999) and σ_{pei} is the Peierls stress (see
163 values in Table 1).
164 Due to the occurrence of non-Newtonian creep mechanisms, Equation (6) is generally non-linear. We
165 thus employ a local iteration method (Popov & Sobolev, 2008; Schmalholz & Duretz, 2017) that ensures
166 correct additive decomposition of the strain rate tensor and computation of stress tensor.The resulting
167 effective viscosity for dissipative deformation mechanism is equal to the pseudo-harmonic mean of
168 the viscosities of each dissipative deformation mechanism:

$$\eta = \left(\frac{1}{\eta^{\mathrm{dis}}} + \frac{1}{\eta^{\mathrm{dif}}} + \frac{1}{\eta^{\mathrm{pei}}} + \frac{1}{\eta^{\mathrm{pl}}}\right)^{-1} \quad (15)$$

169 where η^{dis}, η^{dif}, η^{pei} and η^{pl} are the effective viscosities calculated with the corresponding second
170 invariant of strain rate tensor for each deformation mechanism for the viscous and the plastic
171 deformations. In the performed simulations, we apply a minimum cut-off of the viscosity at 10^{19} Pa·s
172 and a maximum cut-off at 10^{25} Pa·s, allowing for viscosities in the models with six orders of magnitude
173 difference.

The applied method allows to calculate iteratively the individual strain rates of each deformation mechanism at a given temperature and total strain rate. Figures 1a-d shows the individual strain rates of each dissipative deformation mechanism, a) dislocation, b) diffusion, c) Peierls creep and d) frictional-plasticity in a temperature versus total strain rate space. We perform these calculations for a temperature range of 300°C to 1'800°C and a total strain rate ranging from 10^{5} to 10^{-50} [1/s] assuming a constant pressure of 1 GPa. Several mechanisms can be active simultaneously (Fig. 1). For illustrative purposes, we apply here a stress of 500 MPa to indicate the limit between the frictional-plastic and viscous domains. In the 2D numerical simulations, the plastic yield stress is pressure-sensitive and varies in space and time. To visualize the dominant deformation mechanism, we compare at each point in the strain rate versus temperature domain the four individual strain rates and identify which mechanism provides the highest strain rate. The mechanism associated with the largest strain rate is the dominant mechanism, as shown in the dominant deformation mechanism map displayed in Figure 1e. Diffusion creep is the dominant mechanism at high temperatures for low strain rates (in orange). Dislocation creep is dominant at high temperatures and higher strain rates (in red). Peierls creep is dominant at low temperature and moderate strain rates (in dark blue) and the plastic domain is dominant at low temperature and high strain rates (in light blue).

2.2 Calculation of slab pull and gravitational potential energy

We quantify two types of forces around subduction zones, one resulting from slab pull force and one resulting from spatial variations of the gravitational potential energy.

We calculate the slab pull force (per unit length) through time with the following integral for a specific time step (approximated by a sum for the numerical calculation):

$$\vec{F}_{\mathrm{SP}} = \int_{H_{\mathrm{Sb}}}^{H_{\mathrm{LAB}}} \Delta\rho \; g dV \approx \sum \Delta\rho \; g \; dx \; dz \; n^{\mathrm{lith}} \qquad (16)$$

where $\Delta\rho$ is the density difference between the density at each point (either the density of the lithosphere or the density of the asthenosphere) and the reference density depth profile on the left

side of the model, and dx and dz are the numerical grid spacings, respectively. We calculate the slab pull only in the asthenosphere, between the bottom of the model (H_{Sb}) and the initial depth of the lithosphere–asthenosphere boundary (H_{LAB}). We consider only numerical cells that include lithospheric material for the calculation of the slab pull force by using the integer n^{lith}, which is 1 for cells including lithospheric material and 0 otherwise.

The gravitational potential energy per unit area (GPE) corresponds to the depth-integrated lithostatic pressure P_L [N/m^2], which is calculated as

$$P_{\mathrm{L}}(x,z) = \int_{z}^{St(x)} \rho(x,z')g\,dz' \tag{17}$$

The GPE is then

$$GPE(x) = \int_{Sb}^{St(x)} P_{\mathrm{L}}(x,z)dz + const \tag{18}$$

where *St(x)* is the topography of the model which can vary in the horizontal (x) direction, z is the depth and *Sb* is the base of the model (for details see Schmalholz et al., 2014). To calculate the topography in our simulations, we apply a numerical algorithm, which includes an Eulerian-Lagrangian free surface implementation, which allows resolving topographic variations at the sub-grid level (Duretz et al., 2016).

The along-profile variation of GPE, ΔGPE, is calculated by subtracting a reference GPE value from all other values. We choose here the GPE value on the left model side as reference value. Along-profile variation of ΔGPE can be due to a horizontal variation of density or a variation of the topography. The ΔGPE provides an estimate for the horizontal driving force per unit length (e.g., Molnar & Lyon-Caen, 1988; Schmalholz et al., 2014; Schmalholz et al., 2019) in the subduction system associated to the density variation at depth due to subduction and to the associated spatial variation of topography. Regions with a negative ΔGPE are under compression and regions with a positive ΔGPE are under extension.

3. - Model configuration

3.1 Configuration of the thermo-mechanical models

The size of the model domain is 3200 km in width and 660 km in height with a numerical resolution of 1 km by 1 km, yielding 2.112 million cells. The time step is calculated according to a Courant criterion of 0.4 in the model. We fixed the initial thickness of the lithosphere to 80 km following the seismic study from Kawakatsu et al. (2009) which localized the lithosphere-asthenosphere boundary (LAB) at this depth for the Pacific lithosphere subducting below Japan. A 5 km thick layer of weak material (cohesion of $1 \cdot 10^6$ Pa and internal friction angle of 0°; see Table 1) is placed on the top of the lithosphere to mimic weak hydrated crust (Crameri et al., 2012). The main aim of this modelling study is to quantify stresses and determine dominant deformation mechanisms in flexural lithospheric regions. Therefore, we apply a simple density and temperature model for the sub-lithospheric region. Initially, the temperature of the asthenospheric mantle (T_{ast}) is homogeneous and for simplicity fixed at 1'450°C. For the temperature of the lithospheric mantle, we consider also for simplicity a linear gradient from 0°C at the surface to the temperature of the asthenospheric mantle (T_{ast}) at the LAB (80 km depth). The initiation of subduction was facilitated by prescribing an oblique weak zone with an initial thickness of 10 km in the horizontal middle of the model (Fig. 2b). The weak zone is characterized by a low plastic strength (see Equation 7 and Table 1) and has the same properties as the weak upper layer.

We use dry olivine for the viscous flow laws of the lithosphere and asthenosphere with the rheological parameters reported in Table 1 (Hirth & Kohlstedt, 2003; Goetze & Evans, 1979 regularized by Kameyama et al., 1999). We employ the dry olivine flow law because the weaker wet olivine is commonly too weak in numerical subduction models and does not generate a coherent slab, but rather generates the dripping of the mantle lithosphere (e.g., Burov, 2010).

We consider two end-member subduction configurations to compare the stress and deformation mechanism in forced and free subduction models. In the forced subduction model, subduction is driven

by a horizontal velocity acting at the sides of the lithosphere. Therefore, the slab velocity is controlled by the applied boundary velocity. In contrast, subduction is only driven by the negative buoyancy of the dense lithosphere in a free subduction model. Therefore, the slab velocity can evolve freely and is controlled by the interaction of buoyancy, flexural and viscous resistance stresses in and around the slab. In the forced subduction model, we apply a symmetrical horizontal velocity on the lithosphere at both sides of the model (Fig. 2b). We choose symmetrical boundary conditions (Chertova, 2012) to have a straight slab as imaged in Japan with tomography (Liu & Zhao, 2016). The total convergence velocity is 10 $cm \cdot yr^{-1}$, as observed in Japan for the Pacific plate (Gripp & Gordon, 1990). These velocity profiles are implemented by specifying a material in-flux in the top part of the model sides until a depth of twice the thickness of the lithosphere. To ensure conservation of the mass, an equivalent out-flux is applied in the lower part of the model sides (Fig. 2b). For the boundary conditions, we use free slip at the model bottom and specific velocity profiles at the left and right model sides (Fig. 2b). At the top of the crust we use a free surface boundary condition (Duretz et al., 2016; Fig. 2b), because previous numerical studies show that the surface topography is controlled by the geometry, rheology and density of the slab (e.g. Zhong & Gurnis, 1994) and that a free surface condition is required to calculate realistic stresses in subducting slabs (Crameri et al., 2017).

For our model configuration (Fig. 2b), subduction will not initiate without horizontal boundary velocities, because there is initially no slab and, hence, no slab pull. Therefore, we initiate subduction in all the simulations with a weak zone in the lithosphere and with external velocities compressing the lithosphere (e.g. Toth & Gurnis, 1998). This model scenario is comparable to the compression-induced mode according to the classification of subduction initiation modes of Stern & Gerya (2018). To initiate free subduction, we first impose boundary velocities and then set the boundary velocities to zero once the slab is large enough to drive subduction without imposed boundary velocities. To constrain the moment when slab pull forces are sufficient to drive subduction, we perform several simulations in which we set the boundary velocities to zero after different simulation times (Fig. 2c), implying the

absence of material flux across lateral boundaries. We also include a weak domain (30 km thick) adjacent to right model boundary, which decouples the lithosphere from the lateral boundary and avoids prescribing a slab-retreat dominated subduction (Fig. 2c). To determine the conditions required for free subduction development, we start the model with forced subduction, save the configuration at different times (Fig. 2a) and then use the saved configurations in the free subduction model to evaluate whether subduction continues or not.

To test the impact of the applied boundary conditions, we also performed two simulations with different boundary conditions: one forced subduction simulation for which the horizontal velocity is only applied at the right model side and one free subduction simulation for which we add a weak zone at both lateral model sides. An overview of the performed simulations is given in Table 2.

3.2 Configuration for the gravity anomaly calculations

With the simulation results we also compute synthetic gravity anomalies in order to compare them with real data, in particular across the Mariana trench. For the gravity anomaly calculations, we use the algorithm of Won & Bevis (1987), based on the method of Talwani et al. (1959). The calculation uses the model geometry and corresponding density field of the numerical mesh at the final time step. To avoid edge effects, the model sides have been extended to great distances (10'000 km each side), which ensures the far-field fit of the gravity field. The topography in our model corresponds to the seafloor, therefore, we add a water layer of 5 km thickness with respect to the far-field, undeformed seafloor with a density of 1'000 $kg \cdot m^{-3}$. We then calculate the gravity contribution of all numerical elements at virtual measurement stations (10 km spacing) at sea-level to obtain a synthetic free-air anomaly profile, which can be then compared to the anomaly profile obtained from natural data.

4. - Results

We performed nine simulations whose characteristics and differences are listed in Table 2. We employed the colour-maps “lapaz” and “vik” of Crameri (2018) for the visualization.

4.1. - Quantification of slab pull force and gravitational potential energy

We first compare three different simulations (Fig. 3) using identical material parameters, namely simulation S0 for forced subduction scenario (Figs. 3a-c) and simulations S1 and S2 for free subduction scenarios (Figs. 3d-i). The only difference between S1 and S2 is the time at which we set the horizontal boundary velocities to zero. The time at which free subduction starts is termed t_{free} and it is equal to 1.25 Ma in S1 and 1.17 Ma in S2. In S0 (Figs. 3a-c), subduction develops with a relative retreat of the trench to the right of the model. This retreat is caused by the velocity imposed on the left side of the box. This trench retreat is not observed in S1 and S2 because no more lithosphere is created on the left side of the box due to the change of boundary conditions (Figs. 3d-i). The evolution of slab geometry differs between models S0 and S1. At the beginning of the simulations (Figs. 3a and d) slabs are similar in both models. The time of these two panels (Figs. 3a and d) is not identical because for S1 we display the first time step of the free subduction simulation, which has a different numerical time step (due to the Courant criterion which is velocity dependent) than the forced subduction simulation. With progressive time, the dip and curvature of the slabs evolve differently. S0 shows a more straight and vertical slab with a smaller curvature in the deeper regions, while S1 shows a slab dip in the opposite direction than the one in the shallower region (Fig. 3f). This curl-type motion is associated with the configuration of the free subduction model, which requires the asthenospheric material to fill the region of the detached slab at the top right region of the model.

Figures 3g-i shows a scenario of a failed model of free subduction development (S2). The only difference between S1 and S2 is the time at which the horizontal boundary velocities are set to zero (t_{free}). These simulations show that the difference between a successful or failed free subduction simulation is linked to the slab pull force, associated only to the negative buoyancy of the slab after

317 t_{free}. To determine the slab pull force required to develop a free subduction in our model configuration
318 and to evaluate the impact of rheological parameters, we first calculate the slab pull force for three
319 different forced subduction simulations (Fig. 4b), namely S0, S4 and S5 (Table 2). In S4 we increased
320 the shear modulus to $G = 3 \cdot 10^{13}$ Pa, in order to decrease the impact of elasticity, and in S5 we reduced
321 the friction angle to 5°. The three simulations show a similar increase of the slab pull force as function
322 of time up to ca. 4 Ma (Fig. 4b). After 4 Ma, S5 differs from the other two simulations and shows a
323 larger slab pull for the same time. We apply several free subduction starting times (t_{free} corresponding
324 to squares and circles in Fig. 4a) for the reference forced subduction simulation S0 in order to evaluate
325 the required slab pull force for free subduction (Fig. 4a). For the applied model configuration, a slab
326 pull force larger than 1.8 TN·m^{-1} is required to develop a free subduction in the case of S0. The time to
327 generate this slab pull force in S0 is ca. 1.15 Ma using a horizontal boundary velocity of 5 cm·yr^{-1} at
328 each side of the model. If the slab pull is not large enough before the horizontal boundary velocities
329 are set to zero, then the subduction slows down and ceases, temperature conduction heats up the
330 slab, as illustrated by the shift of the isotherm for 1'440°C in the asthenosphere (Fig. 3h), and the base
331 of the lithosphere starts to delaminate. In contrast, when slab pull is larger than 1.9 TN·m^{-1} in S0, the
332 subduction continues. The vertical velocities associated with the delamination for a failed free
333 subduction model are significantly slower than velocities of the subducting slab (compare times in Figs.
334 3c, f and i).
335 The quantification of along-profile variations of GPE, ΔGPE, in the lithosphere–asthenosphere system
336 allows quantifying the along-profile variation of horizontal driving forces in the system. Hence, regions
337 under overall horizontal compression or extension are identified and the corresponding horizontal
338 forces are quantified. To investigate these forces around the modelled subduction system, we quantify
339 the relative contribution of (i) density variations below the initial lithospheric thickness due to
340 subduction and (ii) topography variations due to lithospheric flexure to ΔGPE. To quantify
341 contributions due to sub-lithospheric density variations we calculate ΔGPE by integrating P_L from the

342 model bottom up to a depth of 80 km, the initial lithosphere thickness. The relative variation of the
343 total ΔGPE and the topography agree in the right side of the subduction trench for both forced and
344 free subduction model (Figs. 5 and 6). This agreement indicates that the variation of total ΔGPE is
345 controlled by the variation of topography created by the flexure of the lithosphere, and that the flexure
346 of the subducting plate does not affect the density field below the lithosphere. In contrast, relative
347 variations of total ΔGPE and the topography on the upper plate side of the trench do not agree. If a
348 significant slab has developed, then the variation of total ΔGPE on the upper plate side of the trench
349 agrees with the ΔGPE beneath 80 km because the variation in total ΔGPE is there controlled by deep
350 density variations due to subduction of the cold slab. The GPE calculation shows that the subduction
351 system is characterized by three regions with respect to ΔGPE variations and associated horizontal
352 driving forces: (1) extensional horizontal driving forces related to the flexural bulge of the subducting
353 plate, (2) compressive horizontal driving forces in the trench region associated to the negative
354 topography of the trench region and (3) extensional horizontal driving forces in the overriding plate
355 region related to deep density variations caused by the subducted plate (Figs. 5 and 6). The maximal
356 difference in total *GPE* for the forced subduction is ca. 80 TN/m and for the free subduction ca. 110
357 $TN{\cdot}m^{-1}$ (Fig. 5c and 6c). The division of these values by the model height of 660 km provides a minimum
358 estimate for the vertical average of the horizontal differential stress caused by subduction-related
359 variations of GPE. These vertically-averaged horizontal differential stresses are ca. 121 MPa and 167
360 MPa for the forced and free subduction, respectively. These vertically-averaged differential stresses
361 are required to maintain the subduction zone and to avoid that the subduction system disappears
362 immediately and returns to a state of static equilibrium, which is characterised by vertical density
363 variations only and no topography.
364

4.2. - Analyses of strain rate, deformation mechanisms, effective viscosity and horizontal deviatoric stress

Strain rate

We quantify the strain rate field with the square root of the second invariant of the deviatoric strain rate tensor, $\dot{\varepsilon}_{II}$, for the forced (Figs. 7a-c, S0) and the free subduction model (Figs. 7d-f, S1). High values of $\dot{\varepsilon}_{II}$ indicate regions of intense deformation whereas low values indicate regions of little deformation. The distribution and magnitude of $\dot{\varepsilon}_{II}$, hence, indicates, for example, whether the deformation around a subduction system and within the slab is either more or less homogeneous or strongly heterogeneous. For both S0 and S1 the strain rates in the upper region of the lithosphere are small away from the subduction zone (Fig. 7). These low strain rate regions feature high viscosity, dominantly elastic deformation (see following sections, Figs. 9 and 10) and an essentially rigid, plate-like behaviour. In S0, strain rates are generally highest in the lower region of the lithosphere and in the upper regions of the asthenosphere (Figs. 7a-c). These high strain rates are due to the applied horizontal boundary velocity profile, which move material into the model domain in the upper model region and, to conserve mass, move material out of the model in the lower regions (see Fig. 2b). For S1, the strain rates in the upper plate region, in the front of the subducting slab, are significantly smaller because no material in- and out-flow is considered (Figs 7d-f). However, strain rates are also high in the lower regions of the subducting plate (right model region) where the underlying asthenosphere is being sheared by the subducting plate (Figs. 7d-f).

Deformation mechanisms

To study the relative importance of the five modelled deformation mechanisms, namely elastic deformation, frictional-plastic deformation, diffusion creep, dislocation creep, and Peierls creep we plot the individual strain rates for each deformation mechanism separately using Equation (6) (Fig. 8). Figure 8a shows the total strain rate corresponding to the results shown in Figure 7c for S0. Strain rates due to elastic deformation are significant in the upper regions of the lithosphere in the subduction

zone (Fig. 8b). Strain rates due to frictional-plastic deformation are significant (i) in the weak zone between the overriding and subducting plate and (ii) in the uppermost region of the subducting plate where the plate starts to subduct (Fig. 8c). This region corresponds to the outer hinge zone of the subducting plate. In the lower region of the lithosphere and upper region of the asthenosphere, both diffusion and dislocation creep are significant (Figs. 8d and e). Strain rates due to dislocation creep are generally higher than the ones for diffusion creep. High strain rates due to dislocation creep are in the mantle lithosphere and in the mantle wedge corner (Fig. 8e). Strain rates caused by Peierls creep are significant only (i) in small areas in the region where the plate subducts and (ii) in a small area around the hinge region of the subducting plate (Fig. 8f). Around the subduction zone, each of the five deformation mechanisms is dominant in some region (Fig. 8g). Therefore, all five deformation mechanisms are important for lithosphere deformation around the subduction zone. For comparison, the corresponding effective viscosity field is also shown (Fig. 8h). Upper regions of the lithosphere with high effective viscosity correspond generally to regions in which elastic deformation is dominant. Low viscosity regions correspond to regions in which dislocation and diffusion creep is dominant.

Considering the entire model domain, the distribution of dominant deformation mechanism is similar for S0 and S1 (Fig. 9) except for dislocation creep. The deformation associated with dislocation creep corresponds to the region with the highest strain rate in Fig. 7. Frictional-plastic deformation is dominant in three different regions: in a thin zone (ca. 5 km thick) on the top of the lithosphere corresponding to the model weak crust, in the triangular weak zone mimicking an accretionary prism between the subducting and overriding plates, and in the outer hinge zone caused by flexure of the downgoing slab. In this hinge zone, frictional-plastic deformation associated with the development of normal-fault-type shear zones propagates downwards to ca. 30 km depth. Elastic deformation is dominant in the upper regions of the lithosphere down to a depth of ca. 60 km, measured orthogonally from the top of the lithosphere. Elastic deformation is dominant in the subducting slab to depths of more than 500 km (Figs 9c and f).

Effective viscosity

The effective viscosity has contributions from all the considered viscous and plastic deformation mechanisms and thus depends on the strain rate, temperature and pressure. Since these quantities vary in space and time, it is not trivial to predict lithospheric regions, which are mechanically strong or weak, or to predict the absolute values of the effective viscosity. In our simulations, the effective viscosity varies by six orders of magnitude (Fig. 10). The viscosity below the lithosphere, in regions unaffected by the subducted slab, exhibits an increase as function of increasing pressure with depth. This increase from ca. 10^{19} to 10^{22} Pa·s at the base of the model is due to the increase of pressure with depth controlled by the activation volume, *V* (Table 1). Overall, the effective viscosity distribution is similar for S0 and S1.

Horizontal deviatoric stress

To identify regions in horizontal compression or extension and to quantify stress magnitudes we analyse the distribution of the horizontal deviatoric stress, τ_{xx}. The bending of the slab around the subduction zone causes flexural stresses and this bending also generates a topographic high, the so-called flexural fore-bulge, in the slab region in front of the subduction zone (e.g., Turcotte and Schubert, 2014). Therefore, we also analyse in the following this topographic bulge to assess how much topographic variation is associated with the calculated stress distribution and magnitudes. The link between surface topography and rheological behaviour of the subducting slab has been also demonstrated by previous studies (e.g., Zhong & Gurnis, 1994; Crameri et al., 2017). Absolute values of τ_{xx} are largest in the upper part of the lithosphere where the subducting lithosphere is bending and is colder (Fig. 11). During the initial stages of subduction, both S0 and S1 show the characteristic pattern of bending (e.g. Burov, 2011; his figure 5), or flexure, around the hinge zone of the subducting plate (Figs. 11a and d). The outer hinge region is under extension (positive τ_{xx}) and the inner hinge

region is under compression (negative τ_{xx}). When subduction evolves and slabs become longer, the plate straightens back, or unbends, causing a stress pattern in the opposite sense (Figs. 11c and f; e.g. Faccenda et al., 2012): the upper part of the lithosphere is under compression and the lower part under extension.

In S0, the horizontal regions of the subducting plate are under compression during the initial stages of subduction (Fig. 11a). With progressive subduction, the stress state of the horizontal region changes from compression to extension and extensive values of τ_{xx} become larger with progressive subduction (Figs. 11b and c). This change in stress state is likely due to the increasing slab pull, which starts pulling the subducting plate once it is larger than the compressive stresses due to the applied boundary velocities. The orientation and magnitude of the principal stresses, σ_1 and σ_3, confirm the result of distribution of τ_{xx} (Figs. 11g and h). If the horizontal regions of the lithosphere are in compression, then σ_1 is approximately horizontal (Fig. 11g). For extension, σ_3 is horizontal. The orientation of the principal stresses shows that these principal stresses are always either parallel or orthogonal to the local dip of the subducting plate so that the strong regions of the slab act as a stress guide (Figs. 11g and h).

Impact of elasticity

Rocks generally deform visco-elastically, and the time scale over which elastic stresses are relaxed can be estimated to the first order by the so-called Maxwell relaxation time, which is the ratio of the effective viscosity to the shear modulus, η/G. Using 10^{23} Pa·s as representative, average effective viscosity for the slab and $3{\cdot}10^{10}$ Pa for *G* provides a relaxation time of ca. 100 kyr. One could, therefore, argue that elastic stresses are largely relaxed during subduction processes with durations of several millions of years and that, hence, elasticity might not be important for slab deformation during subduction (e.g., Schmeling et al., 2008). To study the impact of elasticity in our models, we performed two forced subduction simulations: one with a shear modulus, G in Equation (6), which is two orders

of magnitude larger than in the reference simulation, i.e. $3 \cdot 10^{12}$ Pa, and one with a shear modulus, which is three orders of magnitude larger than in the reference simulation, i.e. $3 \cdot 10^{13}$ Pa (Fig. 12). In the simulations with unrealistically high shear modulus of $3 \cdot 10^{12}$ and $3 \cdot 10^{13}$ Pa the elastic behaviour is significantly less dominant because the Maxwell relaxation time, during which elastic stresses relax, is significantly shorter (e.g., Jaquet et al., 2016).

We compare the topography of the subducting plate from the three numerical simulations with the analytically calculated flexural geometry fitting the Mariana trench (Turcotte & Schubert, 2014) and obtain reasonable agreement (Fig. 12a). However, the height of the flexural bulge, ca. 800 m, is higher in the reference simulation than in the simulations with $G = 3 \cdot 10^{12}$ Pa and $G = 3 \cdot 10^{13}$ Pa, ca. 400 m. The lateral topographic variation around the bulge region is considerably smaller in the simulations with unrealistically high values of G, indicating that elasticity has a strong impact on the flexural behaviour in the bulge region. The depth of the trench is similar for the three simulations.

The overall distribution of the horizontal deviatoric stress, τ_{xx}, in the subducting plate is similar for the three simulations (Fig. 12 b to d). However, the absolute values of τ_{xx} are smallest for the reference simulation and the reduction of the impact of elasticity increases stress values (Figs. 12b-d). In the simulation with $G = 3 \cdot 10^{13}$ Pa, the overriding plate exhibits significant larger compressive stresses than in the simulation with a standard elastic shear modulus. The regions dominated by elastic deformation are replaced mostly by the frictional-plastic deformation mechanism when the impact of elasticity is reduced (Figs. 12e-g), except in the deeper regions of the subducting lithosphere where elastic deformation is replaced by Peierls creep (Figs. 12e-g). The results show that the implementation of elasticity significantly affects both the magnitude of stresses and the distribution of non-elastic deformation mechanisms.

Impact of friction angle

The absolute magnitudes of stress, especially maximal values, in the mantle lithosphere are still contentious. One reason for this is that different laboratory flow laws for mantle rocks predict stresses that can be up to one order of magnitude different for the same temperature, strain rate and pressure (e.g., Mei et al., 2010; Jain et al., 2017). Furthermore, different authors apply stress cut-offs in the mantle, for example, to match tectonic plate size distribution in mantle convection simulations (e.g., Mallard et al., 2016) or apply reduced friction angles (≤ 15°), which further reduce with progressive plastic strain (down to 2°), in order to indirectly consider the weakening effects of fluids or other strain softening mechanisms (e.g., Erdős et al., 2014). Moreover, since the effective friction angle depends on fluid pressure, the appropriate friction angle for the mantle lithosphere is debated and, hence, different friction angles are often used for the mantle lithosphere in numerical models of subduction (e.g., Li et al., 2010). To test the impact of absolute stress magnitudes, we performed two more simulations with a reduced friction angle for the lithosphere (Fig. 13). The friction angle is reduced to limit maximal stress values but not to mimic any particular natural process. The standard value for the friction angle is 30° and we decrease this angle to 5° (Figs. 13c and f) and 1° (Figs. 13d and g) in the two additional simulations. The reduction of friction angle changes the topographic profiles around the flexural bulge of the subducting plate (Fig. 13a). A friction angle to 5° generates a shorter flexural wavelength whereas a friction angle of 1° does not generate a realistic flexural topography at all. These results are in broad agreement with results of Crameri et al. (2017) who, amongst others, also show a larger bulge and flexural wavelength with larger friction angle (their figure S10).

The reduction of friction angles reduces, as expected, the maximal absolute values of τ_{xx} (Figs. 13b-d) and changes the distribution of dominant deformation mechanism (Figs. 13e-g). In the simulation with a friction angle of 1° a continued subduction cannot be established because the slab is thinned in the trench region and detaches, or breaks-off (Fig. 13g). The reduction of stress magnitudes makes the slab mechanically so weak that the slab pull force cannot be transmitted anymore to the horizontal

513 regions of the lithosphere, the slab pull cannot drive horizontal plate motion anymore so that the slab
514 detaches. For a friction angle of 5° maximal absolute deviatoric stress magnitudes are between 50 and
515 100 MPa. Also, for a friction angle of 5° the region with dominant frictional-plastic deformation is
516 significantly larger than for a friction angle of 30° (Fig. 13e and f). Particularly, the region of slab
517 unbending (between 50 and 100 km depth and 200 km < x < 250 km in Fig. 13f) shows significant
518 firctional-plastic deformation, which is not the case for a friction angle of 30° (between 50 and 100 km
519 depth and 200 km < x < 250 km in Fig. 13e). Maximal absolute deviatoric stress magnitudes of a few
520 hundred MPa seem to be required in order to generate a flexural wavelength corresponding to the
521 Mariana trench, as is the case in the model with standard elastic shear modulus.
522
523 ### Impact of boundary conditions
524 We have also performed a forced subduction simulation (S7, Table 2) and a free subduction simulation
525 (S8) using different boundary conditions than in reference models (S0, S1). In S7 we apply a horizontal
526 velocity only at the right model side, but with a value of 10 $cm \cdot yr^{-1}$ so that the absolute convergence
527 velocity is identical to the one of S0. After ca. 2.8 Ma the stress field and the slab geometry are similar
528 for S0 and S7 (Fig. 14a and c). However, after ca. 4 Ma the slab geometry and, hence, the associated
529 stress field are different (Fig. 14b and d). In S8 we apply a weak zone at both lateral model sides so
530 that the slab and overriding plate can detach from both lateral model sides. After ca. 6.9 Ma and ca. 8
531 Ma both simulations S1 and S8 exhibit a similar slab geometry and stress field. These additional
532 simulations indicate that the applied boundary conditions have a significant impact on the forced
533 subduction simulations but not on the free subduction simulations.
534
535 ## 5. – Discussion
536 The deformation behaviour, the thermal structure and the mineral composition of the lithosphere are
537 only approximately known and, hence, published numerical subduction models commonly differ in

538 terms of the applied flow laws, temperature and density fields. Our models were not designed to
539 closely match a specific subduction system and we used standard rheological models, and simple
540 density and temperature fields. However, we assume that our mathematical model, the model
541 configuration, the applied boundary conditions, the temperature field, the densities and the applied
542 rheological model, including the different creep flow laws, generate a subduction process, which
543 should be comparable, to the first order, to a natural ocean-ocean subduction system. To test whether
544 the modelled effective deformation behaviour, such as flexure of the slab, and the modelled slab pull,
545 controlled by the model density field, are indeed in broad agreement with natural observations, we
546 compare our model results with a major subduction system, namely with real data from the Mariana
547 subduction zone. We chose the Mariana trench because it is a prominent subduction zone and has
548 been frequently used for the comparison with mathematical subduction models (e.g., Funiciello et al.,
549 2003; Turcotte & Schubert, 2014). We first compare topography of the ocean floor to assess the
550 flexural behaviour of the lithosphere. Secondly, we compare modelled gravity anomalies with
551 anomalies derived from data measured in the field in order to assess the density field (Figs. 15 and 16).
552 For the topography comparison, we use the seafloor topography data from the Mariana trench
553 (Funiciello et al., 2003; Turcotte & Schubert, 2014). For the visual comparison between natural and
554 calculated topography profiles, we have used the position of the trench (x = 0) as a reference (Fig. 15).
555 The first-order topography of both forced and free subduction models fits the natural topography and
556 the analytical solution of Turcotte & Schubert (2014). Therefore, the applied flow laws and rheological
557 behaviour of our model lithosphere, controlling the height of the flexural bulge and the flexural
558 wavelength, broadly agree with the flexural behaviour of a natural oceanic lithosphere.
559 For the gravimetric comparison, we use the global WGM2012 model for free-air gravity anomaly,
560 which has a resolution of 2'x2' (Bonvalot et al., 2012), and compare it with the synthetic free-air gravity
561 anomalies calculated for our model density field (Fig. 16). We extract ten gravity anomaly profiles
562 perpendicular to the trench from the WGM2012 (Fig. 16a). From the numerical models, we calculate

two free-air anomaly profiles, one for the forced and one for the free subduction model (Fig. 16b). For comparison, we have co-located all gravity anomaly profiles at the trench (Fig. 16b). Our modelled free-air gravity anomalies agree with the long-wavelength variation of the observed anomaly. Modelled anomalies exhibit a similar width and amplitude in their spatial variation compared with the natural free-air gravity anomalies. The shorter wavelength variations and peaks in the natural gravity anomalies are due to the natural seafloor topography, reflecting the formation and deformation of the volcanic arc to the West of the Mariana trench and the seamounts to the East on the Pacific plate (Fig. 16a). These peaks vary across the selected 10 observed profiles and our model has not aimed at reproducing such short wavelength variations.

The comparison of model and natural topography allows evaluating the applicability of the modelled flexural behaviour of the lithosphere to nature. This modelled flexural behaviour and the associated topography is controlled by the considered deformation mechanisms, the flow laws and material parameters (e.g. Zhong & Gurnis, 1994; Crameri et al., 2017). Consequently, the topography comparison allows evaluating whether the employed flow laws and material parameters are applicable to natural cases. However, since natural topography can vary significantly between different subduction zones, different subduction zones likely exhibit different rheological and density characteristics (e.g., Crameri et al., 2019). The free surface implementation is therefore, well suited for the comparison of model and natural topography. A modelled free surface topography is also essential for the calculation of along-profile variations of ΔGPE (Figs. 5 and 6). The topography controls gravity anomalies, which further depend on the density field. We calculate the density with an equation of state (EOS), which depends on T and P (see Equation 4). We do not consider mineral phase transformation, which could affect the localization of deformation in this compressive setting (e.g., Hetényi et al., 2011). The comparison of gravity anomaly profiles from our model with natural free-air gravity anomaly profiles obtained across the Mariana trench shows that both of our model density fields are appropriate; at least for the considered natural subduction zone (Fig. 16). Our simulations

588 show differences in the forced and free subduction models. However, with respect to topography (e.g.,
589 bulge) or gravity anomalies, these differences are not significant (Figs. 15 and 16). The maximal
590 amplitude of the modelled gravity anomaly profile for the free subduction model is larger than the one
591 for the forced subduction model. However, considering the lateral variability of natural gravity
592 anomaly profiles across the Mariana trench, both models fit the natural data to a good level.
593 Alternative to gravity anomalies, ΔGPE profiles show larger differences between forced and free
594 subduction models, because for a more vertical slab the ΔGPE anomaly is narrower (Figs. 5 and 6).
595
596 The calculated stress field (Fig. 11) shows that the subducting plate's outer bend of the hinge zone is
597 under extension and the inner bend is under compression. This deformation distribution is expected
598 for the subducting plate, but our model allows quantifying the contribution of individual deformation
599 mechanism. The flexural behaviour varies along the subducting plate and in the downgoing plate the
600 outer region of the plate is under compression and the inner one under extension (Fig. 11). This
601 variation of flexural behaviour along the subducting slab is in agreement with analytical results of Ribe
602 (2010) who shows that the sign of the rate of curvature changes along the slab. Ribe (2010) considered
603 a simpler, linear viscous behaviour of the slab. The comparison with our results, considering five
604 deformation mechanisms and temperature dependent flow laws, indicates that a linear viscous model
605 can capture the first order flexural behaviour of a subducting slab. Regions with high compressive
606 deviatoric stresses of several hundreds of MPa in the downgoing slab next to the subduction interface
607 (Figs 11c and f) can be important for the interpretation of exhumed (ultra-)high pressure rocks.
608 Subducted crustal rock units in the outer regions of subducting slabs could experience high stress and,
609 hence, tectonic overpressure (e.g., Schmalholz & Podladchikov, 2013; Moulas et al., 2019) before they
610 are detached from the subducting plate and return to the surface. If the stress and, hence, the internal
611 resistance of the slab is reduced, then a continuous subduction is not possible anymore because the
612 slab detaches, and the slab pull force cannot be transferred anymore to the horizontal region of the

lithospheric plate (Figs. 13d and g). This behaviour is consistent with the “shallow breakoff” of Duretz et al. (2011a), which systematically occurred for weak slabs (young plates). This result agrees also with predictions of the analytical model of Ribe (2010) who shows that the subduction velocity approaches the Stokes velocity of a detached object when the internal resistance of the slab becomes smaller than the external resistance of the material surrounding the slab.

Stress magnitude and distribution in subducting plates are one of the controlling parameters of intra-slab processes such as earthquakes, metamorphism or fluid transfer. Our results show that in a subducting lithosphere all five considered deformation mechanisms are active and contribute to shape the total stress field (Fig. 8). Particularly, our results show that elastic deformation is the dominant deformation behaviour in large regions of the subducted slab (Fig. 8g). Therefore, models aiming to calculate the intra-plate stress field and intra-plate processes should consider the impact of elastic deformation on the stress field.

Our model results can contribute to a better understanding of the development of faults during plate flexure, and its importance for the hydration of the subducting plate. Several mechanisms have been proposed to bring water from the surface into the mantle, such as bending-related faulting (e.g., Ranero et al., 2003; Faccenda et al., 2008; Faccenda et al., 2009), thermal cracking (Korenaga, 2017) or seismic pumping (Sibson et al., 1975). The length and distribution of faults, which could develop by plate flexure, is therefore important to assess the water budget of the subducting plate. Furthermore, Peacock (2001) suggested that dehydration of antigorite (serpentine) by dehydration reactions could be an explanation for intermediate-depth earthquakes. To constrain the depth of faulting, and therefore the maximum depth where water could be added to the subducting plate is fundamental to test whether part of the earthquakes observed between 15 to 25 km depth could be explained by metamorphic dehydration reaction or not (Peacock, 2001). Our model predicts the formation of faults

638 in the outer hinge zone of the subducting plate (Figs. 8g and 9). These faults develop in a zone of ca.
639 100 km width around the bulge. These frictional-plastic faults reach a depth of ca. 40 km. However,
640 the spatial extent of faulting is highly dependent on the elasticity and plasticity parameters in the
641 model. Figure 12 shows that the extent of plastic deformation changes drastically if the elastic
642 deformation behaviour is modified.
643
644 Flexure of the subducting plate has been also proposed as an important mechanism for the formation
645 of petit-spot volcanoes (Hirano et al., 2006). Petit-spot volcanoes represent small volumes of alkaline
646 magmas that have been emitted on the top of the downgoing Pacific plate in front of Japan (Hirano et
647 al., 2006). These magmas are emitted 300 to 600 km away from the trench, which could correspond
648 to the region where the plate starts to bend (Hirano et al., 2006). Petit-spot volcanoes are, therefore,
649 interpreted as the products of deformation-driven melt segregation of melt initially present at the base
650 of the lithosphere. Since their first observation in front of Japan, petit-spot volcanoes have been
651 identified in several subduction zone, such as Tonga (Hirano et al., 2008), Chile (Hirano et al., 2013),
652 and Sunda trenches (Taneja et al., 2015), or as an accreted petit-spot in Costa Rica (Buchs et al., 2013).
653 These observations suggest that petit-spot volcanism is a global process around subduction zones. In
654 this context, the deformation behaviour and its changes along the lithosphere-asthenosphere
655 boundary are critical to understand how low degrees of volatile rich melts can be extracted from the
656 base of the lithosphere. Earlier models suggest that large flexural curvatures imposed on the pre-flexed
657 lithosphere might instigate brittle fracturing even at the base of the lithosphere (Hirano et al., 2006;
658 Yamamoto et al., 2014). Our Figure 8g shows, however, that deformation around the base of the
659 lithosphere (from 50 km depth to the LAB) is likely controlled by diffusion and dislocation creep.
660 Propagation of brittle faults down to the base of the lithosphere is, therefore, unlikely. Consequently,
661 percolation of melts within the basal viscous region of the lithosphere, before its extraction by faults
662 when the melts reach the elastic domain, seems a more realistic model for petit-spot formation. A

663 possible mechanism of melt transport in the viscous region could be ascent in the form of porosity
664 waves (e.g., Connolly & Podladchikov, 2007). The viscous percolation model is in agreement with
665 recent multiple saturation laboratory experiments which show that petit-spot melts equilibrate last
666 with the mantle phases (olivine, orthopyroxene, and clinopyroxene) at pressures between 1.8 and 2.1
667 GPa and at temperatures around 1'280–1'290°C, which are P-T conditions corresponding to the
668 lithosphere rather than the top of the asthenosphere (Machida et al., 2017). Another argument in
669 favour for the ascent and equilibration of low degree melts at the base of the lithosphere is the
670 presence in petit-spot lavas with xenoliths showing evidence of metasomatic enrichment (Pilet et al.,
671 2016). One important question concerning petit-spot formation is which process or parameter initiates
672 melt percolation in the basal part of the lithosphere. The porosity at the base of the lithosphere is
673 frequently considered as too small to allow for silicate melt percolation. Our numerical model allows
674 quantifying the extension produced by plate flexure. Figure 11 suggests that the base of the
675 lithosphere where the plate starts to bend is slightly in extension, but the effect is very limited at
676 depths greater than 50 km where absolute magnitudes of τ_{xx} are significantly less than 10 MPa.
677 Nevertheless, the current model considers a homogeneous dry-olivine lithology and future models
678 considering additionally wet or higher-porosity domains at the base of the lithosphere, i.e., in the low
679 seismic velocity zone, will be important to constrain the effect of plate flexure on the stress state at
680 the base of the lithosphere.
681

682 ## 6. - Conclusions

683 We performed 2D thermo-mechanical numerical simulations of subduction, considering both forced
684 and free subduction regimes as well as a composite rheological model including elasticity, frictional-
685 plasticity, diffusion, dislocation and Peierls creep. In the forced subduction regime, we initiate
686 subduction by applying horizontal boundary velocities. The initiation by a forced subduction must
687 generate an embryonic slab to continue a free subduction simulation, for which boundary velocities

688 are set to zero and subduction is driven by buoyancy forces of the slab. For our configuration, the
689 embryonic slab should produce a slab pull force (per unit length) of at least 1.8 $TN \cdot m^{-1}$ so that free
690 subduction can occur.
691 We show that the five employed deformation mechanisms are all important for the evolution of the
692 subducting lithospheric plate for both forced and free subduction. Particularly, elastic deformation is
693 important because it affects the flexural behaviour, the magnitude and distribution of deviatoric
694 stresses and the distribution of dominant deformation mechanisms. Simulations with an unrealistic,
695 reduced impact of elasticity show significantly larger stress magnitudes and larger regions with high
696 stresses in the subducting and overriding plate than corresponding simulations with appropriate
697 elasticity. For our model configuration, the simulations with elasticity also fit best the natural flexural
698 bulge and wavelength of the Mariana subduction zone. Therefore, including elasticity in numerical
699 subduction models seems important for an appropriate calculation of stresses, of the distribution of
700 deformation mechanisms and of flexure in a subduction system.
701 We also show that a subduction system generates along-profile variations of GPE corresponding to
702 horizontal driving forces in the lithosphere-asthenosphere system. These GPE variations result from
703 either topography variations associated to plate flexure or from deeper density variations caused by
704 subduction of the lithosphere into the asthenosphere. For both forced and free subduction models the
705 GPE variations cause compressive forces in the trench region and extensive forces in front and behind
706 the trench region. These latter likely have strong impact on driving petrological processes such as melt
707 migration across the lithosphere, at significant distance from the trench.
708 Although our models were not specifically designed for reproducing a particular subduction zone, the
709 simulation results closely match natural seafloor topography and free-air gravity anomalies across the
710 Mariana trench. This fit indicates that our model density field and the applied rheological model
711 generate buoyancy and flexural stresses in agreement with this particular natural subduction zone.
712 Calculated maximal absolute values of deviatoric stresses in the bending and subducting lithosphere

713 are approximately 500 MPa. If absolute magnitudes of maximal deviatoric stresses are significantly less
714 than 100 MPa, caused for example by a reduced friction angle, continuation of subduction does not
715 occur because the denser subducting slab detaches from the lithosphere. Hence, deviatoric stress
716 magnitudes of several hundreds of MPa are required for a continuous subduction. The uppermost
717 region of the oblique, subducting slab shows high compressive stress, due to unbending, directly next
718 to the subduction interface. Such high compressive stress may affect metamorphic reactions in rock
719 units before they are detached from the subducting slab and exhumed to the surface.
720

721 **Acknowledgements**

722 We thank Fabio Crameri and an anonymous reviewer for very helpful and constructive reviews. This
723 work was supported by the University of Lausanne.
724

725 ## References

726

727

728 Babeyko, A.Y., Sobolev, S.V, 2008. High-resolution numerical modeling of stress distribution in visco-
729 elasto-plastic subducting slabs, *Lithos*, **103(1-2)**, 205-216. doi.org/10.1016/j.lithos.2007.09.015
730 Bonvalot, S., Balmino, G., Briais, A., Kuhn, M., Peyrefitte, A., Vales, N., Biancale, R., Gabalda, G.,
731 Reinquin, F., Sarrailh, M., 2012. World Gravity Map. Commission for the Geological Map of the World.
732 Eds. BGI-CGMW-CNES-IRD, Paris.
733 Buchs, D.M., Pilet, S., Cosca, M., Flores, K.E., Bandini, A.N., Baumgartner, P.O., 2013. Low-volume
734 intraplate volcanism in the Early/Middle Jurassic Pacific basin documented by accreted sequences in
735 Costa Rica, *Geochem. Geophys. Geosyst.*, **14**, 1552–1568. doi.org/10.1002/ggge.20084

736 Burov, E.B., 2010. The equivalent elastic thickness (Te), seismicity and the long-term rheology of
737 continental lithosphere: time to burn-out “crème brûlée”?: insights from large-scale geodynamic
738 modelling, *Tectonophysics*, **484(1-4)**, 4-26. doi.org/10.1016/j.tecto.2009.06.013
739 Burov, E.B., 2011. Rheology and strength oft he lithosphere, *Marine and Petroleum Geology*, **28**, 1402-
740 1443. doi.org/10.1016/j.marpetgeo.2011.05.008
741 Chertova, M.V., Geenen, T., van den Berg, A., Spakman, W., 2012. Using open sidewalls for modelling
742 self-consistent lithosphere subduction dynamics, *Solid Earth*, **3**, 313-326. doi.org/10.5194/se-3-313-
743 2012
744 Čížková , H., van Hunen, J., van den Berg, A., 2007. Stress distribution within subducting
745 slabs and their deformation in the transition zone, *Phys. Earth planet. Inter.*, **161(3-4)**, 202–214.
746 doi.org/10.1016/j.pepi.2007.02.002
747 Connolly, J.A.D., Podladchikov, Y.Y, 2007. Decompaction weakening and channeling instability in
748 ductile porous media: Implications for asthenospheric melt segregation, *J. geophys. Res: Solid Earth*,
749 **112**, B10205. doi.org/10.1029/2005JB004213
750 Crameri, F., Tackley, P.J., Meilick, I., Gerya, T.V., Kaus, B.J.P., 2012. A free plate surface and weak
751 oceanic crust produce single-sided subduction on Earth, *Geophysical Research Letters*, **39(3)**, L03306.
752 doi.org/10.1029/2011GL050046
753 Crameri, F., Lithgow-Bertelloni, C.R., Tackley, P.J., 2017. The dynamical control of subduction
754 parameters on surface topography, *Geochem. Geophys. Geosyst.*, **18**, 1661-1687.
755 doi.org/10.1002/2017GC006821
756 Crameri, F., 2018. Scientific colour-maps. Zenodo. http://doi.org/10.5281/zenodo.1243862
757 Crameri, F., Conrad, C.P., Montési, L., Lithgow-Bertelloni, C.R., 2019. The dynamic life of an oceanic
758 plate, *Tectonophysics*, **760**, 107-135. doi.org/10.1016/j.tecto.2018.03.016

759 Duretz, T., Gerya, T.V., May, D.A., 2011. Numerical modelling of spontaneous slab breakoff and
760 subsequent topographic response, *Tectonophysics*, **502**, 244–256.
761 doi.org/10.1016/j.tecto.2010.05.024
762 Duretz, T., May, D.A., Gerya, T.V., Tackley, P.J., 2011. Discretization errors and free surface stabilization
763 in the finite difference and marker-in-cell method for applied geodynamics: A numerical study,
764 *Geochem. Geophys. Geosyst.*, **12**, Q07004. doi.org/10.1029/2011GC003567
765 Duretz, T., Gerya, T.V., Spakman, W., 2014. Slab detachment in laterally varying subduction zones: 3-D
766 numerical modelling, *Geophys. Res. Lett.*, **41**, 1951–1956. doi.org/10.1002/2014GL059472
767 Duretz, T., May, D.A., Yamato, P., 2016. A free surface capturing discretization for the staggered grid
768 finite difference scheme, *Geophys. J. Int.*, **204**, 1518–1530. doi.org/10.1093/gji/ggv526
769 Erdős, Z., Huismans, R.S., van der Beek, P., Thieulot, C., 2014. Extensional inheritance and surface
770 processes as controlling factors of mountain belt structure, *J. geophys. Res.: Solid Earth*, **119(12)**, 9042-
771 9061. doi.org/10.1002/2014JB011408
772 Faccenda, M., Burlini, L., Gerya, T.V., Mainprice, D., 2008. Fault-induced seismic anisotropy by
773 hydration in subducting oceanic plates, *Nature*, **455**, 1097–1100. doi.org/10.1038/nature07376
774 Faccenda, M., Gerya, T.V., Burlini, L., 2009. Deep slab hydration induced by bending-related variations
775 in tectonic pressure, *Nat. Geosci.*, **2**, 790–793. doi.org/10.1038/ngeo656
776 Faccenda, M., Gerya, T. V., Mancktelow, N. S., Moresi, L., 2012. Fluid flow during slab unbending and
777 dehydration: Implications for intermediate-depth seismicity, slab weakening and deep water recycling,
778 *Geochem. Geophys. Geosyst.*, **13(1)**, Q01010. doi.org/10.1029/2011GC003860
779 Farrington, R.J., Moresi, L.-N., Capitanio, F.A., 2014. The role of viscoelasticity in subducting plates,
780 *Geochem. Geophys. Geosyst.*, **15**, 4291-4304. doi.org/10.1002/2014GC005507
781 Funiciello, F., Morra, G., Regenauer-Lieb, K., Giardini, D., 2003. Dynamics of retreating slabs: 1. Insights
782 from two-dimensional numerical experiments, *J. geophys. Res.: Solid Earth*, **108(B4)**, 2206.
783 doi.org/10.1029/2001JB000898

Garel, F., Goes, S., Davies, D., Davies, J.H., Kramer, S.C., Wilson, C.R., 2014. Interaction of subducted slabs with the mantle transition-zone: A regime diagram from 2-d thermomechanical models with a mobile trench and an overriding plate, *Geochem. Geophys. Geosyst.*, **15**, 1739–1765. doi.org/10.1002/2014GC005257

Gerya, T., 2011. Future directions in subduction modeling. *J. Geodyn.*, **52**, 344–378. doi.org/10.1016/j.jog.2011.06.005

Gerya, T., 2019. Introduction to Numerical Geodynamic Modelling, 2nd ed. Cambridge University Press, Cambridge. doi.org/10.1017/9781316534243

Goetze, C., Evans, B., 1979. Stress and temperature in the bending lithosphere as constrained by experimental rock mechanics, *Geophys. J. Int.*, **59**, 463–478. doi.org/10.1111/j.1365-246X.1979.tb02567.x

Gripp, A.E., Gordon, R.G., 1990. Current plate velocities relative to the hotspots incorporating the NUVEL-1 global plate motion model, *Geophys. Res. Lett.*, **17**, 1109–1112. doi.org/10.1029/GL017i008p01109

Gurnis, M., Hall, C., Lavier, L., 2004. Evolving force balance during incipient subduction, *Geochem. Geophys. Geosyst.*, **5**, Q07001. doi.org/10.1029/2003GC000681

Hassani, R., Jongmans, D., Chéry, J., 1997. Study of plate deformation and stress in subduction processes using two-dimensional numerical models, *J. geophys. Res.: Solid Earth*, **102(B8)**, 17951-17965. doi.org/10.1029/97JB01354

Hetényi, G., Godard, V., Cattin, R., Connolly, J.A.D., 2011. Incorporating metamorphism in geodynamic models: the mass conservation problem, *Geophys. J. Int.*, **186(1)**, 6-10. doi.org/10.1111/j.1365-246X.2011.05052.x

Holt, A.F., Becker, T.W., Buffett, B.A., 2015. Trench migration and overriding plate stress in dynamic subduction models, *Geophys. J. Int.*, **201(1)**, 172-192. doi.org/10.1093/gji/ggv011

808 Hirano, N., Takahashi, E., Yamamoto, J., Abe, N., Ingle, S.P., Kaneoka, I., Hirata, T., Kimura, J.-I., Ishii, T.,
809 Ogawa, Y., Machida, S., Suyehiro, K., 2006. Volcanism in Response to Plate Flexure, *Science New Series*,
810 **313**, 1426–1428. doi.org/10.1126/science.1128235
811 Hirano, N., Koppers, A.A.P., Takahashi, A., Fujiwara, T., Nakanishi, M., 2008. Seamounts, knolls and
812 petit-spot monogenetic volcanoes on the subducting Pacific Plate, *Basin Res.*, **20**, 543–553.
813 doi.org/10.1111/j.1365-2117.2008.00363.x
814 Hirano, N., Machida, S., Abe, N., Morishita, T., Tamura, A., Arai, S., 2013. Petit-spot lava fields off the
815 central Chile trench induced by plate flexure, *Geochem. J.*, **47**, 249–257.
816 doi.org/10.2343/geochemj.2.0227
817 Hirth, G., Kohlstedt, D., 2003. Rheology of the Upper Mantle and the Mantle Wedge: A View from the
818 Experimentalists. In Inside the Subduction Factory, J. Eiler (Ed.). doi.org/10.1029/138GM06
819 Jain, C., Korenaga, J., Karato, S.I., 2017. On the yield strength of oceanic lithosphere. *Geophysical*
820 *Research Letters*, **44(19)**, 9716-9722. doi.org/10.1002/2017GL075043
821 Jaquet, Y., Duretz, T., Schmalholz, S.M., 2016. Dramatic effect of elasticity on thermal softening and
822 strain localization during lithospheric shortening, *Geophys. J. Int.*, **204**, 780–784.
823 doi.org/10.1093/gji/ggv464
824 Kameyama, M., Yuen, D.A., Karato, S.-I., 1999. Thermal-mechanical effects of low-temperature
825 plasticity (the Peierls mechanism) on the deformation of a viscoelastic shear zone*, Earth planet. Sci.*
826 *Lett.,* **168**, 159–172. doi.org/10.1016/S0012-821X(99)00040-0
827 Kawakatsu, H., Kumar, P., Takei, Y., Shinohara, M., Kanazawa, T., Araki, E., Suyehiro, K., 2009. Seismic
828 Evidence for Sharp Lithosphere-Asthenosphere Boundaries of Oceanic Plates, *Science*, **324**, 499–502.
829 doi.org/10.1126/science.1169499
830 Kearey, P., Klepeis, K.A., Vine, F.J., 2009. Global tectonics, 3rd ed. ed. Wiley-Blackwell, Oxford ;
831 Chichester, West Sussex ; Hoboken, NJ.

832 Korenaga, J., 2017. On the extent of mantle hydration caused by plate bending*, Earth planet. Sci. Lett.,*
833 **457**, 1–9. doi.org/10.1016/j.epsl.2016.10.011
834 Li, Z.H., Gerya, T.V., Burg, J.P., 2010. Influence of tectonic overpressure on P–T paths of HP–UHP rocks
835 in continental collision zones: thermomechanical modelling, *Journal of Metamorphic Geology*, **28(3)**,
836 227-247. doi.org/10.1111/j.1525-1314.2009.00964.x
837 Liu, X., Zhao, D., 2016. P and S wave tomography of Japan subduction zone from joint inversions of
838 local and teleseismic travel times and surface-wave data, *Phys. Earth planet. Inter.*, **252**, 1-22.
839 doi.org/10.1016/j.pepi.2016.01.002
840 Machida, S., Kogiso, T., Hirano, N., 2017. Petit-spot as definitive evidence for partial melting in the
841 asthenosphere caused by CO2, *Nat. Commun.*, **8**, 14302. doi.org/10.1038/ncomms14302
842 Mallard, C., Coltice, N., Seton, M., Müller, R.D., Tackley, P.J., 2016. Subduction controls the distribution
843 and fragmentation of Earth's tectonic plates, *Nature*, **535**, 140-143. doi.org/10.1038/nature17992
844 Mei, S., Suzuki, A.M., Kohlstedt, D.L., Dixon, N.A., Durham, W.B., 2010. Experimental constraints on
845 the strength of the lithospheric mantle, *J. geophys. Res.: Solid Earth*, **115**, B08204.
846 doi.org/10.1029/2009JB006873
847 Molnar, P., Lyon-Caen, H., 1988. Some simple physical aspects of the support, structure, and evolution
848 of mountain belts, in: Clark, S.P., Jr., Burchfiel, B.C., Suppe, J. (Eds.), Processes in Continental
849 Lithospheric Deformation. Geological Society of America. doi.org/10.1130/SPE218-p179
850 Molnar, P., England, P., Martinod, J., 1993. Mantle dynamics, uplift of the Tibetan Plateau, and the
851 Indian Monsoon, *Rev. Geophys.*, **31(4)**, 357–396. doi.org/10.1029/93RG02030
852 Moresi, L., Dufour, F., Mühlhaus, H.-B., 2003. A Lagrangian integration point finite element method for
853 large deformation modeling of viscoelastic geomaterials, *J. Computational Physics*, **184(2)**, 476-497.
854 doi.org/10.1016/S0021-9991(02)00031-1

855 Moulas, E., Schmalholz, S.M., Podladchikov, Y.Y., Tajčmanová, L., Kostopoulos, D., & Baumgartner, L.P.
856 2019. Relation between mean stress, thermodynamic, and lithostatic pressure. *Journal of*
857 *metamorphic geology*, **37(1)**, 1-14. doi.org/10.1111/jmg.12446
858 Peacock, S.M., 2001. Are the lower planes of double seismic zones caused by serpentine dehydration
859 in subducting oceanic mantle?, *Geology*, **29**, 299. doi.org/10.1130/0091-
860 7613(2001)029<0299:ATLPOD>2.0.CO;2
861 Pilet, S., Abe, N., Rochat, L., Kaczmarek, M.-A., Hirano, N., Machida, S., Buchs, D.M., Baumgartner, P.O.,
862 Müntener, O., 2016. Pre-subduction metasomatic enrichment of the oceanic lithosphere induced by
863 plate flexure, *Nat. Geosci.*, **9**, 898–903. doi.org/10.1038/ngeo2825
864 Plümper, O., John, T., Podladchikov, Y.Y., Vrijmoed, J.C., Scambelluri, M., 2016. Fluid escape from
865 subduction zones controlled by channel-forming reactive porosity, *Nat. Geosci.*, **10**, 150-156.
866 doi.org/10.1038/ngeo2865
867 Popov, A.A., Sobolev, S.V., 2008. SLIM3D: A tool for three-dimensional thermomechanical modeling of
868 lithospheric deformation with elasto-visco-plastic rheology, *Phys. Earth planet. Inter.*, **171**, 55–75.
869 doi.org/10.1016/j.pepi.2008.03.007
870 Ranero, C.R., Phipps Morgan, J., McIntosh, K., Reichert, C., 2003. Bending-related faulting and mantle
871 serpentinization at the Middle America trench, *Nature*, **425**, 367–373. doi.org/10.1038/nature01961
872 Ribe, N.M., 2010. Bending mechanics and mode selection in free subduction: a thin-sheet analysis,
873 *Geophys. J. Int.*, **180**, 559–576. doi.org/10.1111/j.1365-246X.2009.04460.x
874 Schellart, W.P., Freeman, J., Stegman, D.R., Moresi, L., May, D., 2007. Evolution and diversity of
875 subduction zones controlled by slab width, *Nature*, **446**, 308. doi.org/10.1038/nature05615
876 Schmalholz, S.M., Podladchikov, Y.Y., Schmid, D.W., 2001. A spectral/finite difference method for
877 simulating large deformations of heterogeneous, viscoelastic materials, *Geophys. J. Int.*, **145**, 199–208.
878 doi.org/10.1046/j.0956-540x.2000.01371.x

879 Schmalholz, S.M., Fletcher, R.C., 2011. The exponential flow law applied to necking and folding of a
880 ductile layer, *Geophys. J. Int.*, **184**, 83–89. doi.org/10.1111/j.1365-246X.2010.04846.x
881 Schmalholz, S.M., Podladchikov, Y.Y., 2013. Tectonic overpressure in weak crustal-scale shear zones
882 and implications for the exhumation of high-pressure rocks. *Geophysical Research Letters*, **40(10)**,
883 1984-1988. doi.org/10.1002/grl.50417
884 Schmalholz, S.M., Medvedev, S., Lechmann, S.M., Podladchikov, Y., 2014. Relationship between
885 tectonic overpressure, deviatoric stress, driving force, isostasy and gravitational potential energy,
886 *Geophys. J. Int.*, **197**, 680–696. doi.org/10.1093/gji/ggu040
887 Schmalholz, S.M., Duretz, T., 2017. Impact of grain size evolution on necking in calcite layers deforming
888 by combined diffusion and dislocation creep, *J. Struct. Geol.*, **103**, 37-56.
889 doi.org/10.1016/j.jsg.2017.08.007
890 Schmalholz, S.M., Duretz, T., Hetényi, G., Medvedev, S., 2019. Distribution and magnitude of stress due
891 to lateral variation of gravitational potential energy between Indian lowland and Tibetan plateau,
892 *Geophys. J. Int.*, **216**, 1313–1333. doi.org/10.1093/gji/ggy463
893 Schmeling, H., Babeyko, A.Y., Enns, A., Faccenna, C., Funiciello, F., Gerya, T., Golabek, G.J., Grigull, S.,
894 Kaus, B.J.P., Morra, G., Schmalholz, S.M., van Hunen, J., 2008. A benchmark comparison of
895 spontaneous subduction models—Towards a free surface, *Phys. Earth planet. Inter.*, **171**, 198–223.
896 doi.org/10.1016/j.pepi.2008.06.028
897 Sibson, R.H., Moore, J.Mc.M., Rankin, A.H., 1975. Seismic pumping—a hydrothermal fluid transport
898 mechanism, *J. Geol. Soc.*, **131(6)**, 653–659. doi.org/10.1144/gsjgs.131.6.0653
899 Sobolev, S.V., Babeyko, A.Y., Koulakov, I., Oncken, O., 2006. Mechanism of the Andean orogeny: insight
900 from numerical modelling, *The Andes*. Springer, Berlin, Heidelberg, 513-535.
901 Stern, R.J., 2002. Subduction zones. *Reviews of geophysics*, **40(4)**, 3-1. doi:10.1029/2001RG000108
902 Stern, R.J., Gerya, T., 2018. Subduction initiation in nature and models: A review, *Tectonophysics*, **746**,
903 173–198. doi.org/10.1016/j.tecto.2017.10.014

Talwani, M., Worzel, J.L., Landisman, M., 1959. Rapid gravity computations for two-dimensional bodies with application to the Mendocino submarine fracture zone, *J. Geophys. Res.*, **64(1)**, 49–59. doi.org/10.1029/JZ064i001p00049

Taneja, R., O'Neill, C., Lackie, M., Rushmer, T., Schmidt, P., Jourdan, F., 2015. 40 Ar/ 39 Ar geochronology and the paleoposition of Christmas Island (Australia), Northeast Indian Ocean, *Gondwana Res.*, **28**, 391–406. doi.org/10.1016/j.gr.2014.04.004

Toth, J., Gurnis, M., 1998. Dynamics of subduction initiation at preexisting fault zones, *J. geophys. Res.: Solid Earth*, **103**, 18053–18067. doi.org/10.1029/98JB01076

Turcotte, D., Schubert, G., 2014. Geodynamics, 3rd ed. Cambridge, UK: Cambridge University Press.

Won, I.J., Bevis, M., 1987. Computing the gravitational and magnetic anomalies due to a polygon: Algorithms and Fortran subroutines, *Geophysics*, **52**, 232–238. doi.org/10.1190/1.1442298

Yamamoto, J., Korenaga, J., Hirano, N., Kagi, H., 2014. Melt-rich lithosphere-asthenosphere boundary inferred from petit-spot volcanoes, *Geology*, **42**, 967–970. doi.org/10.1130/G35944.1

Yamato, P., Agard, P., Burov, E., Le Pourhiet, L., Jolivet, L., Tiberi, C., 2007. Burial and exhumation in a subduction wedge: Mutual constraints from thermomechanical modeling and natural P-T-t data (Schistes Lustrés, western Alps) , *J. Geophys. Res.*, **112**, B07410. doi.org/10.1029/2006JB004441

Yamato, P., Husson, L., Braun, J., Loiselet, C., Thieulot, C., 2009. Influence of surrounding plates on 3D subduction dynamics, *Geophys. Res. Lett.*, **36**, L07303. doi.org/10.1029/2008GL036942

Youngs, R.R., Chiou, S.J., Silva, W.J., & Humphrey, J. R., 1997. Strong ground motion attenuation relationships for subduction zone earthquakes. *Seismological Research Letters*, *68*(1), 58-73.

Zhong, S., Gurnis, M., 1994. Controls on trench topography from dynamic models of subducted slabs, *J. geophys. Res.: Solid Earth*, **99(B8)**, 15683-15695. doi.org/10.1029/94JB00809

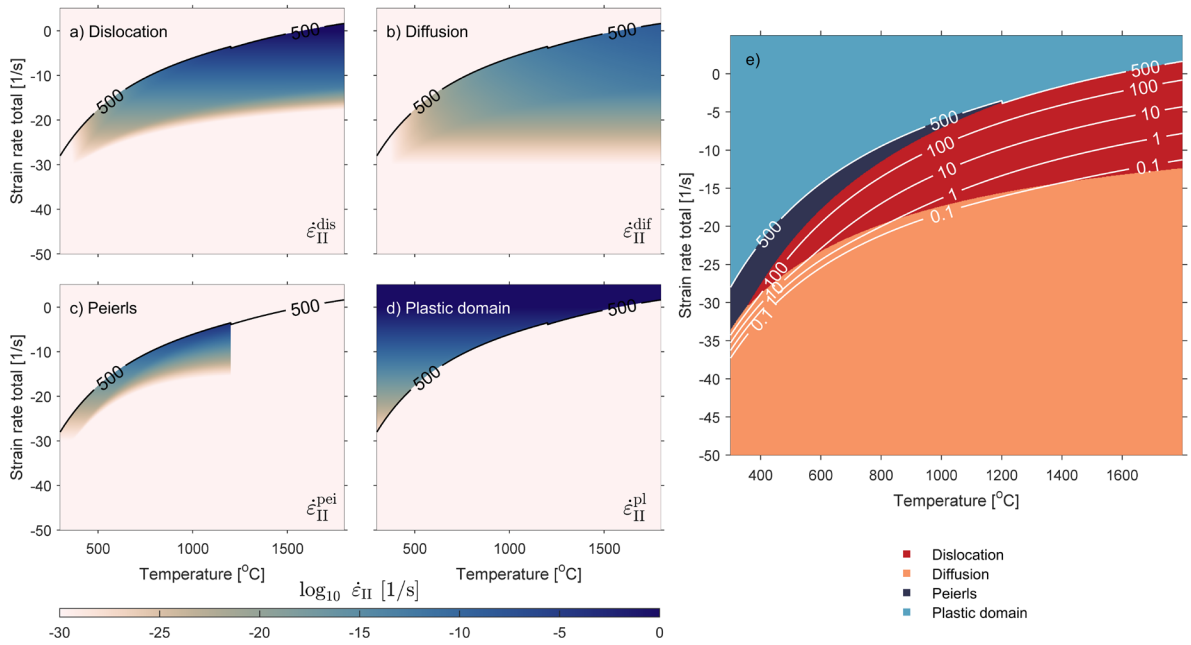

Figure 1. Individual strain rates of dissipative deformation mechanisms for (a) dislocation creep, (b) diffusion creep, (c) Peierls creep and (d) plastic deformation as function of temperature and total strain rate for the applied rheology of the mantle. In panels (a-d), the highest individual strain rates for each deformation mechanism are shown in dark blue, while the slower are in light beige. Calculations made at a pressure of 1 GPa with a grain size of 5 mm. The panel (e) shows the corresponding dominant deformation mechanism map as identified by the legend. The black and white curves are lines of constant stresses with label values in MPa. For illustrative purposes a brittle-plastic yield stress of 500 MPa is assumed.

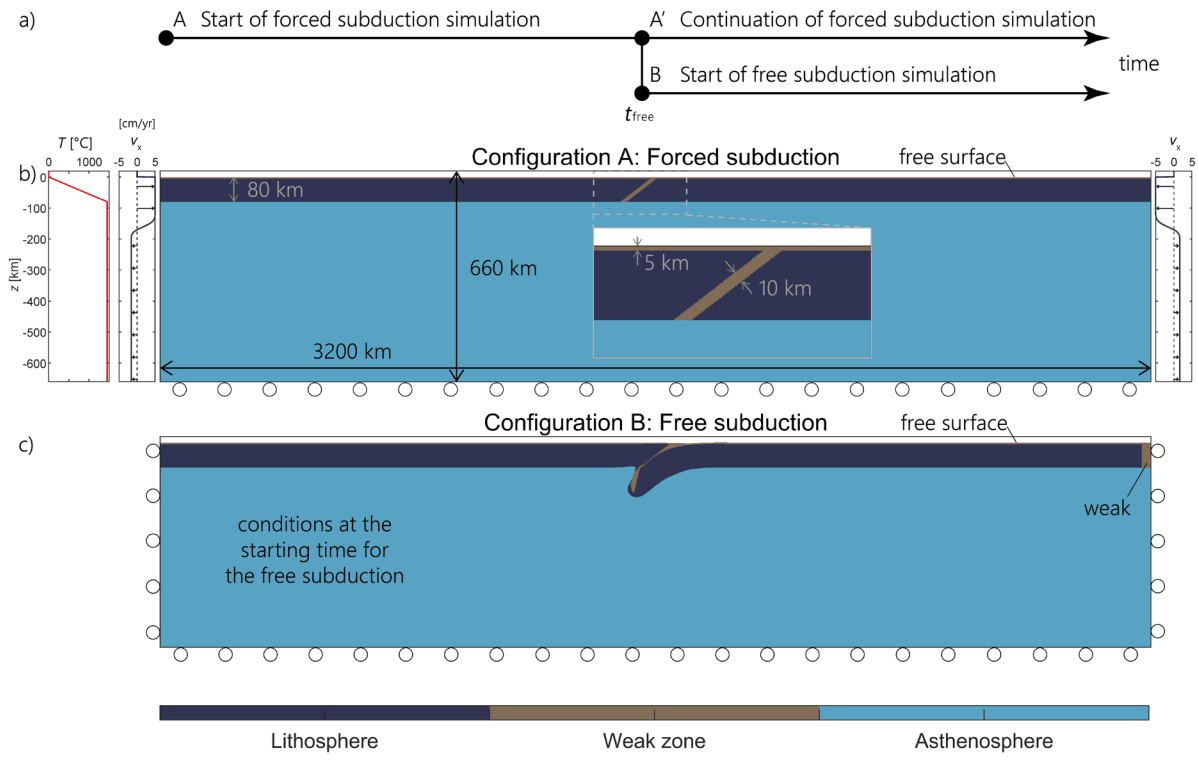

936

937 *Figure 2. Panel (a) shows the time-line sketch of our simulations. Panels (b) and (c) show the model configurations (b) for the*

938 *forced subduction and (c) for the free subduction. Dark blue areas indicate the lithosphere. Brown areas indicate the initial*

939 *weak zone. Light blue areas indicate the asthenosphere. Weak domain's width in panel (c) is 30 km.*

940

941

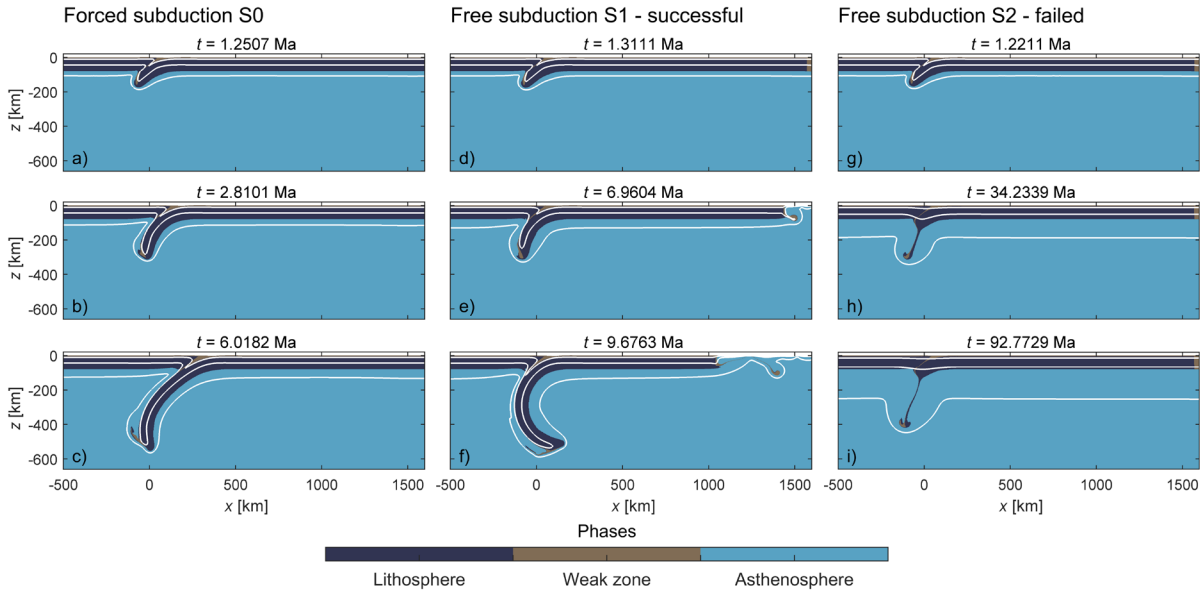

Figure 3. Visualisations of the forced subduction model in panels (a-c), the free subduction model where the subduction continues (successful) with t_{free} = 1.25 Ma in panels (d-f), and the free subduction model where the subduction stops and delaminates (failed) with t_{free} = 1.17 Ma in panels (g-i). Material parameters are identical in all three simulations. The time evolution is chosen for different slab length. Panels (a), (d) and (g) show results for a slab of 75 km, the length of the slab required to initiate the free subduction. Panels (b), (e) and (h) show results for a slab of 310 km and subplots (c), (f) and (i) show results for a slab of 550 km. White lines show the isothermal contours for 200, 800 and 1'440°C.

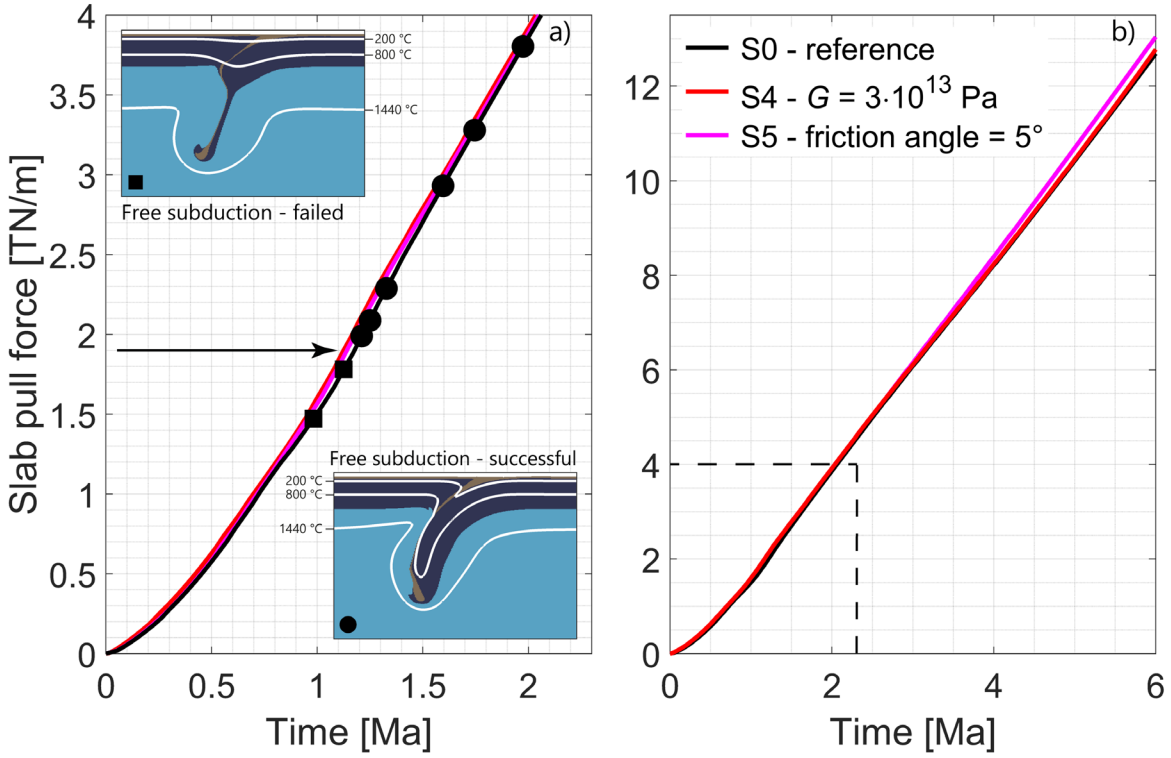

Figure 4. Diagrams showing the evolution of slab pull force with time, panel (a) is a zoom from panel (b). These diagrams evaluates the conditions required to develop a free subduction from the forced subduction simulation of reference S0 (in black). Free subduction simulations start after a period during which plates are pushed until initiation of free subduction. The different points in panel (a) show the slab pull force for different starting times (t_{free}, see Fig. 2a). This t_{free} is the duration of plate push to initiate the subduction in the initial part of the free subduction model simulation. Squares show conditions where free subduction failed, while circles show conditions where free subduction occurs. Black arrow indicates the minimum slab pull force needed to obtain a successful free subduction in S0 model. Inset figures, similar to panels (e) and (h) from Fig. 3, show examples of successful and failed free subduction models. White lines show the isothermal contours for 200, 800 and 1'440°C.

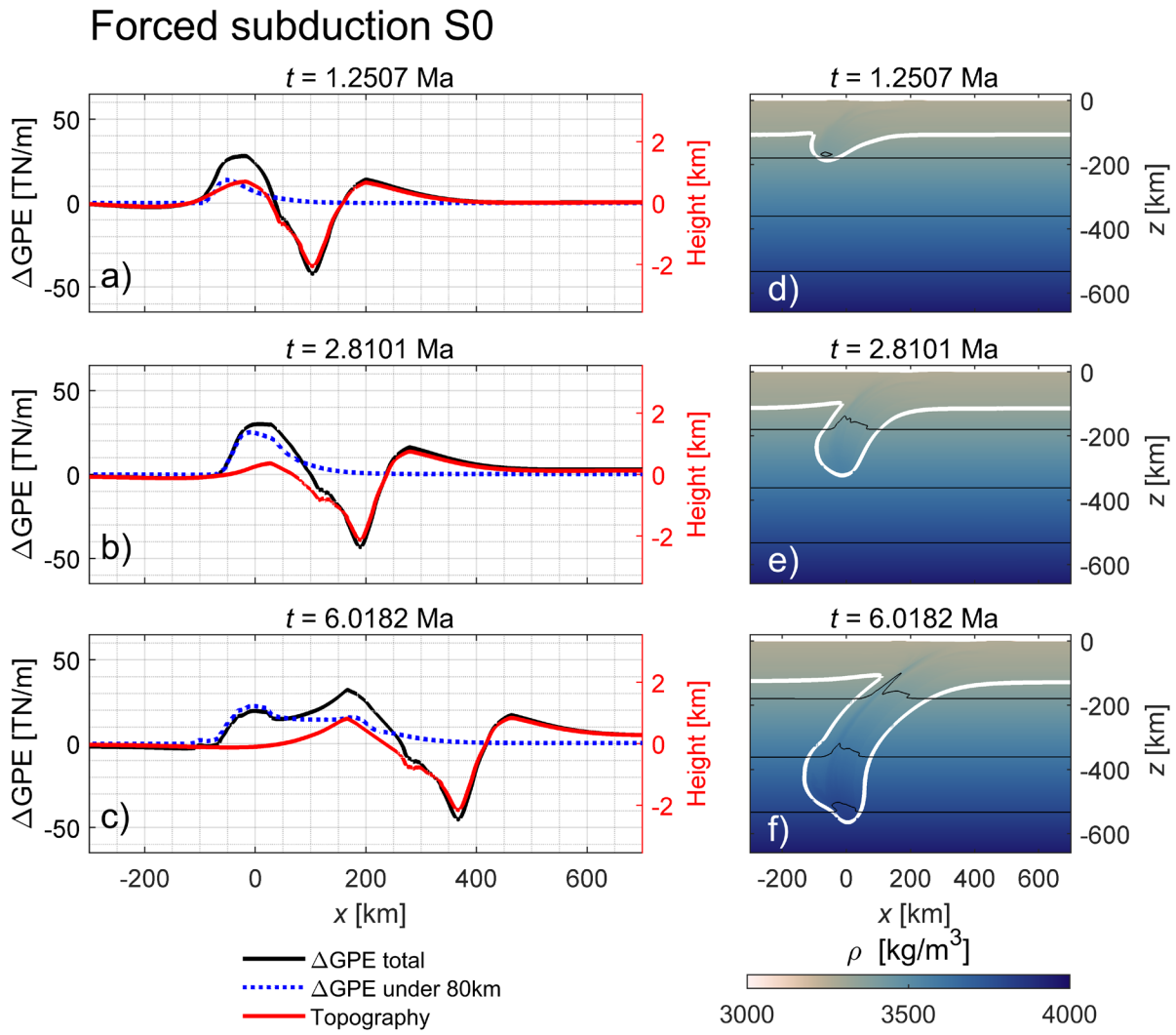

962

963 *Figure 5. Panels (a-c) show the evolution in time, same condition then Figs 3a-c, of the variations of total ΔGPE, ΔGPE beneath*

964 *80 km and topography for the forced subduction model. Vertical left (black) axes are for the ΔGPE values and vertical right*

965 *(red) axes are for topography values. Panels (d-f) show the evolution of density in the region of the subduction zone at*

966 *corresponding model times. White line is a temperature iso-contour for 1'440°C representing the LAB. Black lines are iso-*

967 *contours of density (3'400, 3'600 and 3'800 kg/m³).*

968

969

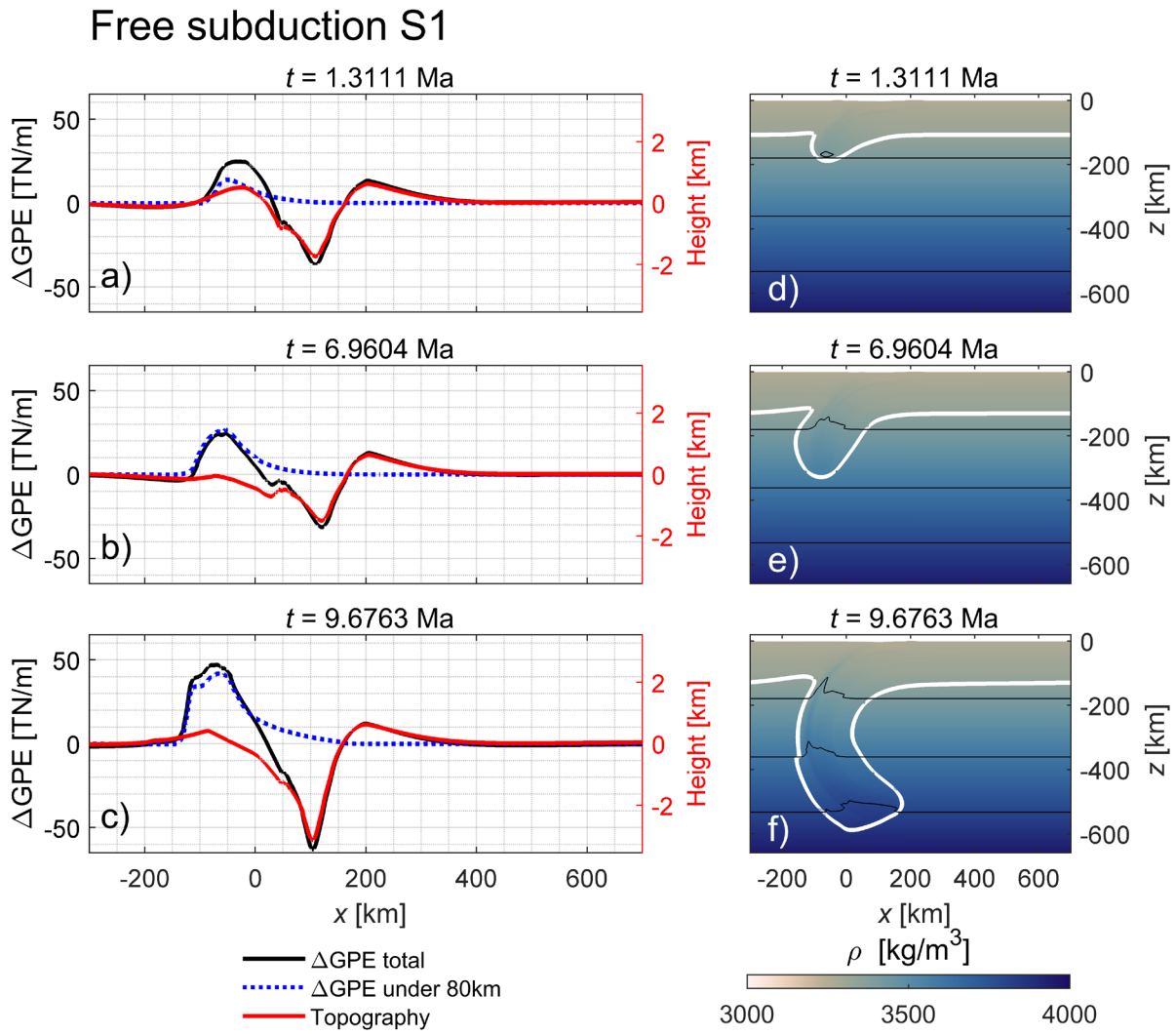

970

971 *Figure 6. Panels (a-c) show the evolution in time, same condition then Figs 3d-f, of the variations of total ΔGPE, ΔGPE beneath*

972 *80 km and topography for the free subduction model. Vertical left (black) axes are for the ΔGPE values and vertical right (red)*

973 *axes are for topography values. Panels (d-f) show the evolution of density in the region of the subduction zone at corresponding*

974 *model times. White line is a temperature iso-contour for 1'440°C representing the LAB. Black lines are iso-contours of density*

975 *(3'400, 3'600 and 3'800 kg/m^3).*

976

977

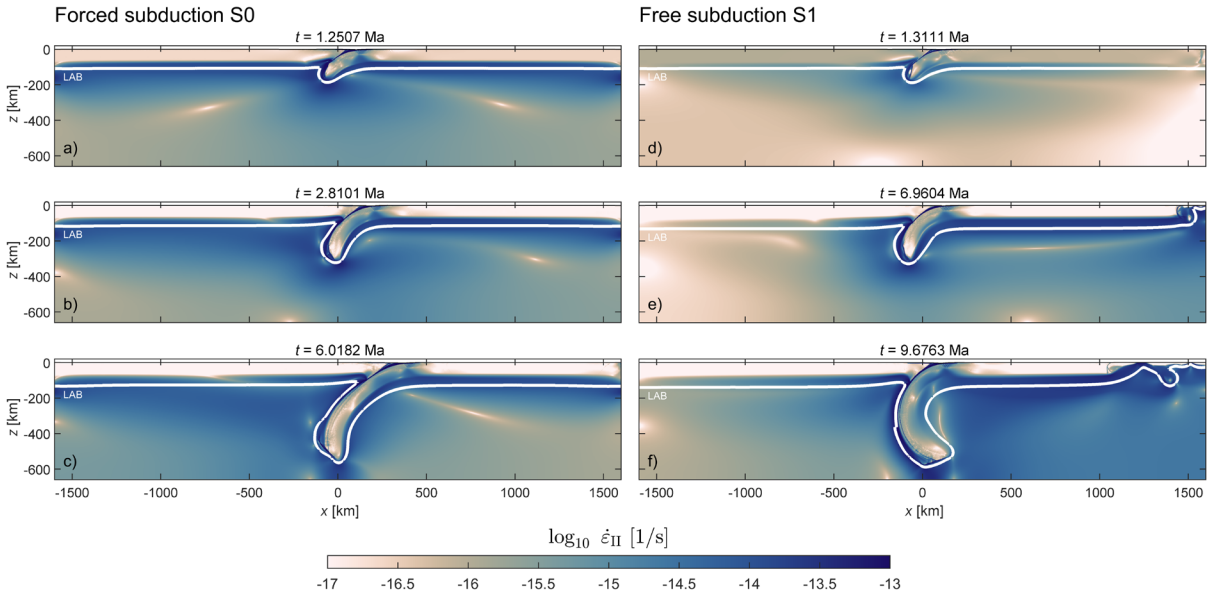

978

979 *Figure 7. Second strain rate invariant evolution for the forced subduction model, (a-c), and for the free subduction model, (d-*

980 *f), same configuration as Figs 3a-f. White lines show the thermally controlled LAB defined as the 1'440°C isotherm.*

981

982

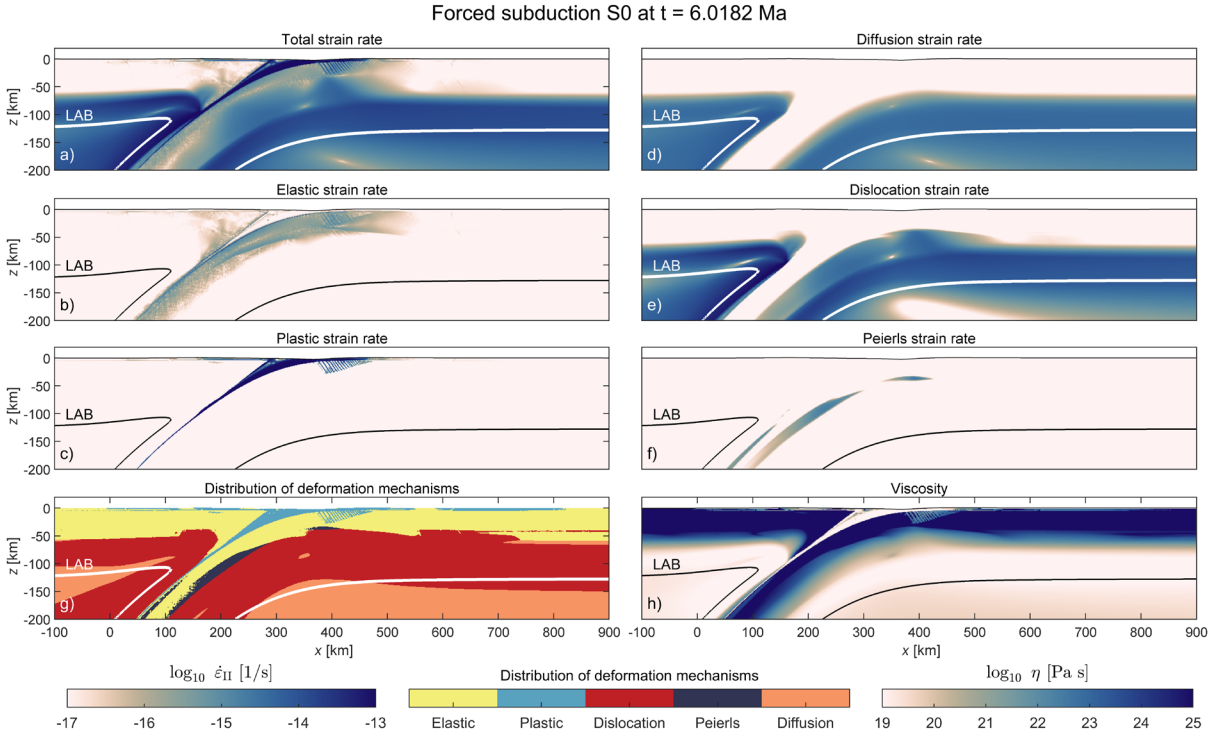

983

984 *Figure 8. Zoom into the subduction zone of the forced subduction model for the time step corresponding to Fig. 7c. In panels*

985 *(a-f) the results of individual strain rates for the different deformation mechanisms are displayed. Panel (a) shows total strain*

986 *rate, (b) elastic strain rate, (c) plastic strain rate, (d) diffusion strain rate, (e) dislocation strain rate and (f) Peierls strain rate.*

987 *Panel (g) shows distribution of deformation mechanism (elastic domain in yellow, plastic domain in light blue, dislocation*

988 *creep in red, Peierls creep in dark blue and diffusion creep in orange) and panel (h) shows effective viscosity (Equation 15).*

989 *White or black lines correspond to the thermally controlled LAB (1'440°C isotherm).*

990

991

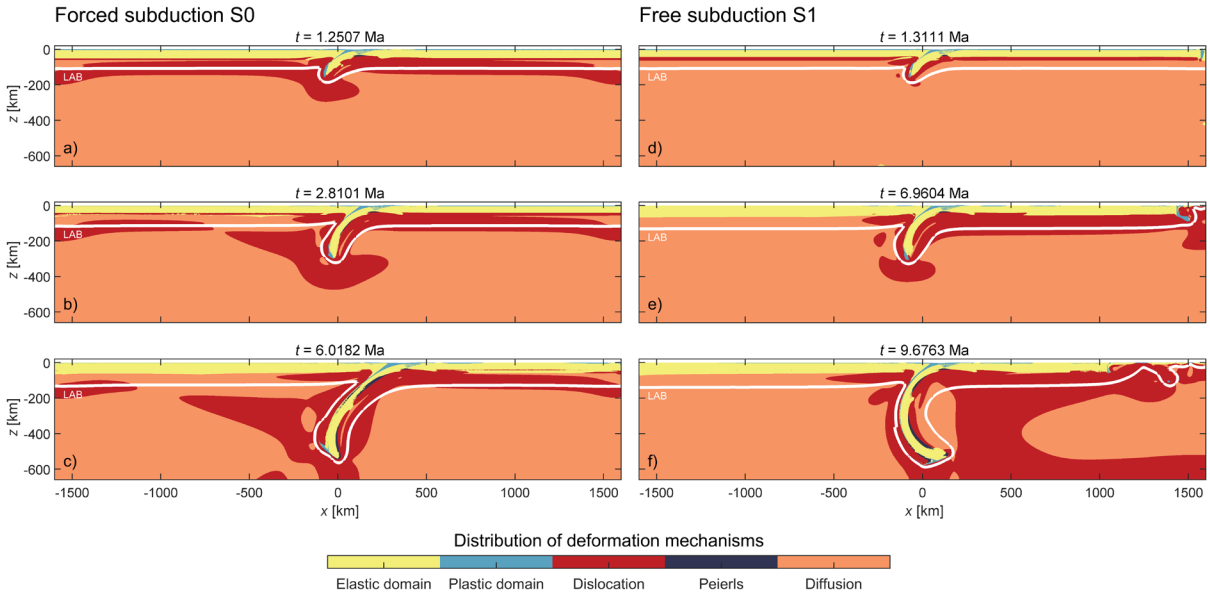

992

993 *Figure 9. Distribution of deformation mechanism evolution for the forced subduction model, (a-c), and for the free*

994 *subduction model, (d-f), same time as Figs 3a-f. White lines correspond to the thermally controlled LAB (1'440°C isotherm).*

995

996

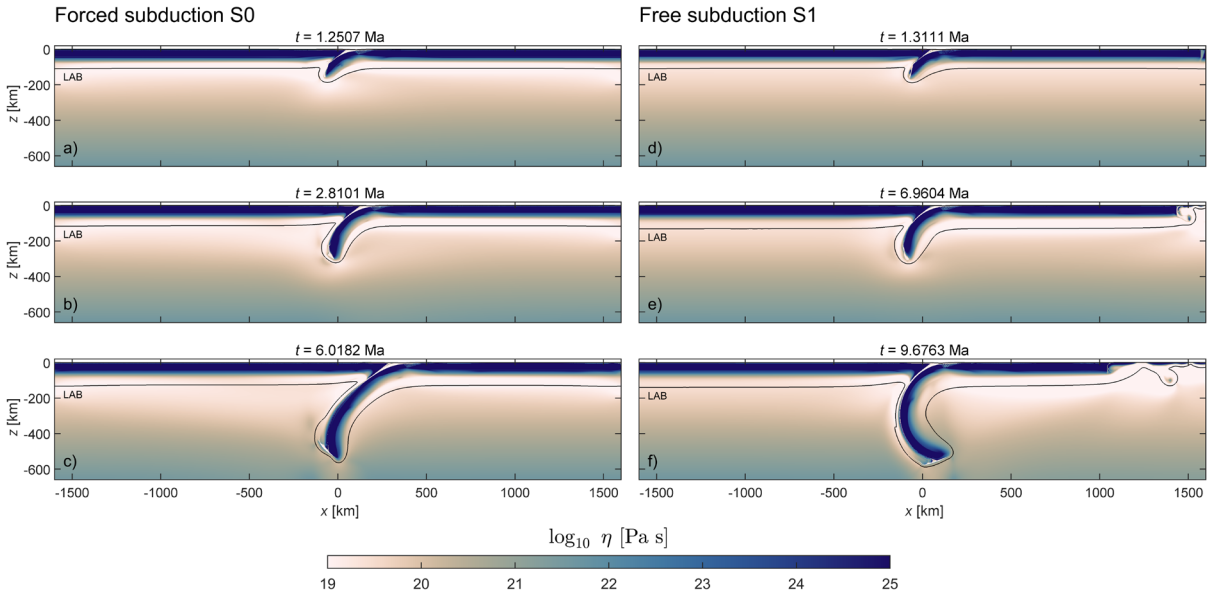

997

998 *Figure 10. Effective viscosity evolution for the forced subduction model, (a-c), and for the free subduction model, (d-f), same*

999 *time as Figs 3a-f. Black lines correspond to the thermally controlled LAB (1'440°C isotherm).*

1000

1001

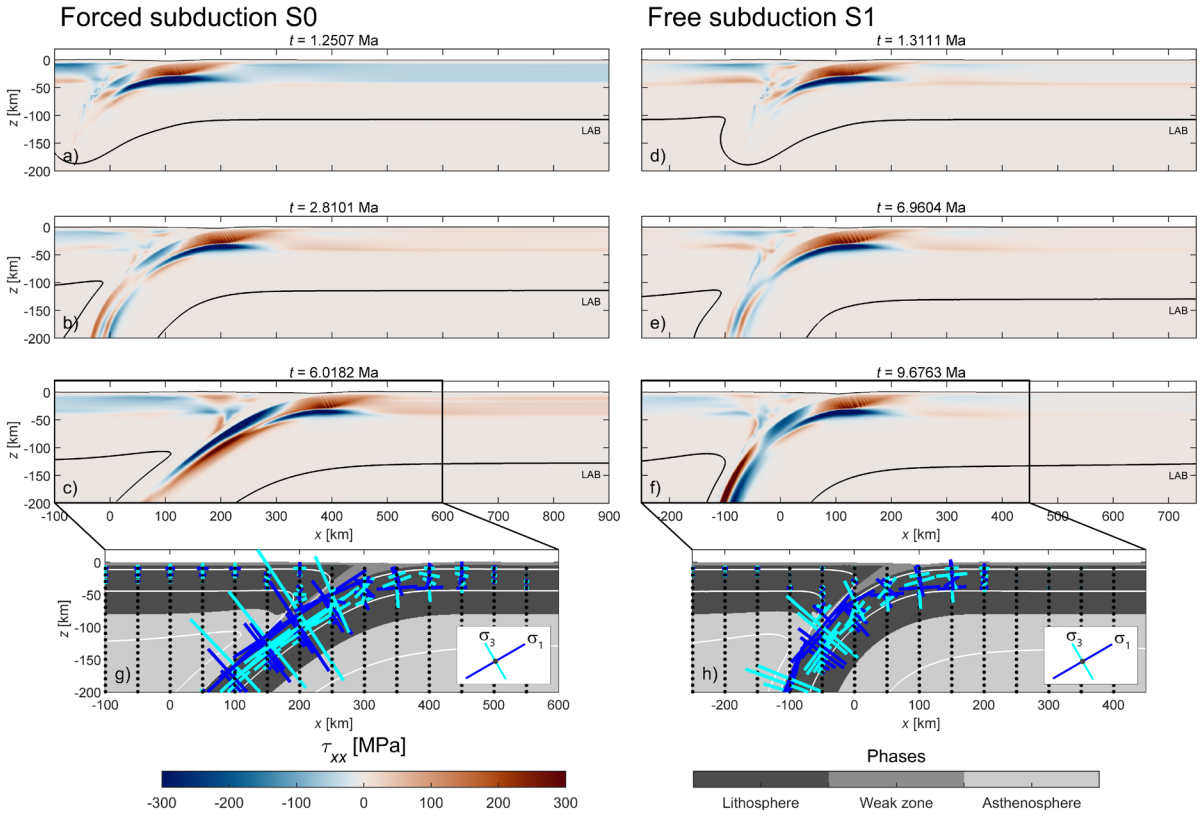

Figure 11. Comparison of horizontal deviatoric stress between the forced subduction model (panels a-c) and the free subduction model (panels d-f) depicted at similar time as Figs 3a-f. Black lines correspond to the thermally controlled LAB (1'440°C isotherm). Areas in red, positive values, show regions associated with extension while areas in blue, negative values, show compression. Panels (g) and (h) show the principal stresses σ_1 in blue and σ_3 in cyan associated, respectively, to panels (c) and (f). The background shows phases and white lines show the isothermal contours for 200, 800 and 1'440°C.

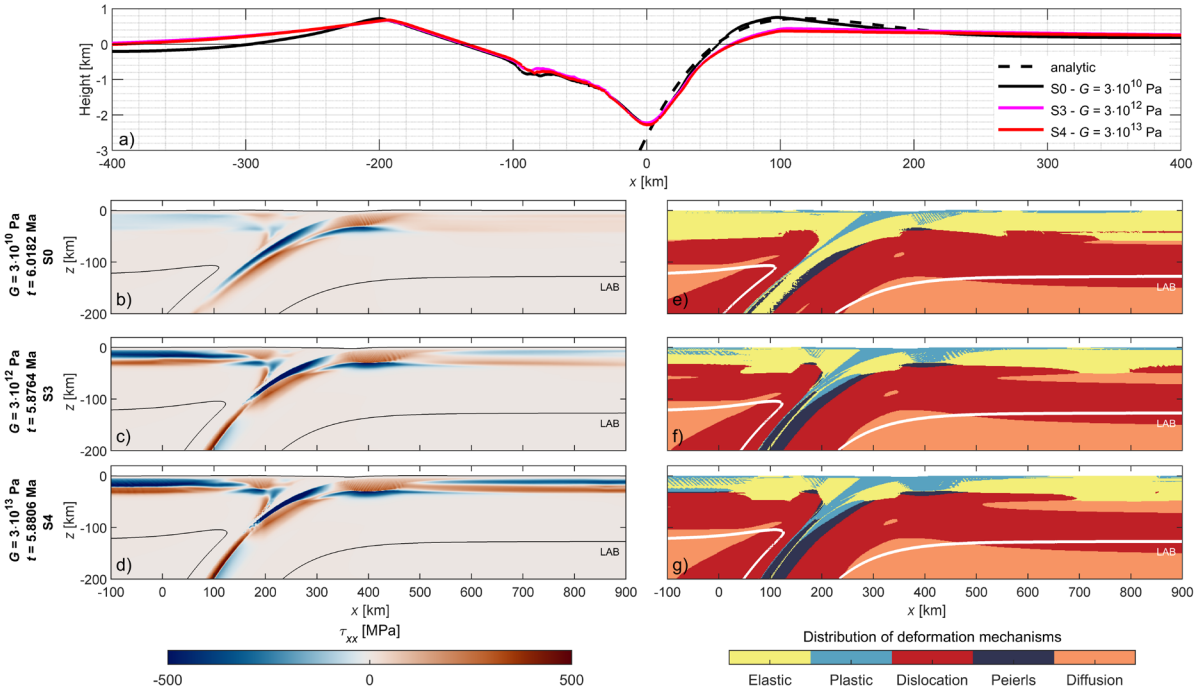

Figure 12. Comparison between three forced subduction models with different elasticity parameters. Results of simulation S0 correspond to the black topography profile in panel (a), the horizontal deviatoric stress in panel (b) and the distribution of deformation mechanisms in panel (e). Results of simulation S3, with an unrealistically high shear modulus of $G = 3 \cdot 10^{12}$, correspond to the pink topography profile in panel (a), the horizontal deviatoric stress in panel (c) and the distribution of deformation mechanisms in panel (f). Results of simulation S4, with an unrealistically high shear modulus of $G = 3 \cdot 10^{13}$, correspond to the red topography profile in panel (a), the horizontal deviatoric stress in panel (d) and the distribution of deformation mechanisms in panel (g). Time step for panels (b) and (e) are the same as in Fig. 3c. Time step for panels (c and f) and (d and g) are chosen to have approximately the same depth of the slab as in panels (b and e) for reference. The dashed line in panel (a) shows the best fit of elastic flexure from the analytical formula from Turcotte & Schubert (2014) (Fig. 3.35 and equation 3.159, $x_b = 55$ km and $w_b = 0.5$ km). In panel (a) the horizontal position of the zero was displaced to match the position of the trench (but not for the other panels). In panels (b-d) areas in red, positive values, show regions associated with extension while areas in blue, negative values, show compression. In panels (b-g) white or black lines correspond to the thermally controlled LAB (1'440°C isotherm).

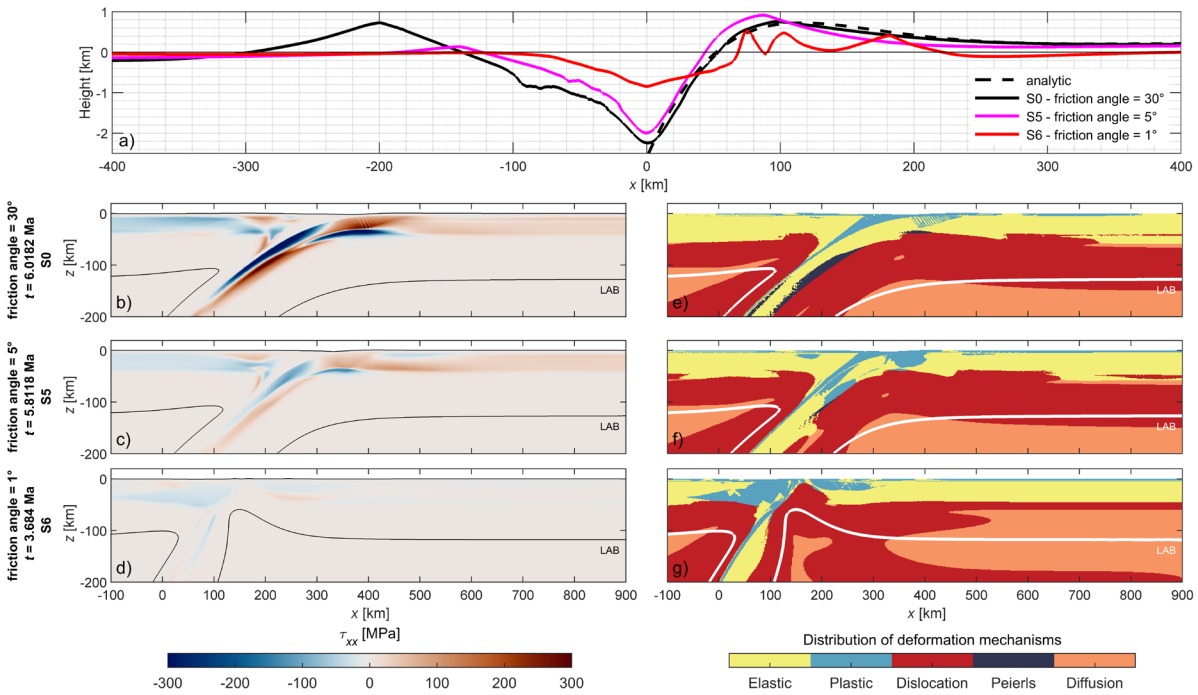

Figure 13. Comparison between three forced subduction models where we change the friction angle of the lithosphere. Results of simulation S0 correspond to the black topography profile in panel (a), the horizontal deviatoric stress in panel (b) and the distribution of deformation mechanisms in panel (e). Results of simulation S5 correspond to the pink topography profile in panel (a), the horizontal deviatoric stress in panel (c) and the distribution of deformation mechanisms in panel (f). Results of simulation S6 correspond to the red topography profile in panel (a), the horizontal deviatoric stress in panel (d) and the distribution of deformation mechanisms in panel (g). Time step for panels (b) and (e) are the same as in Fig. 3c. Time step for panels (c and f) and (d and g) are chosen to have the same depth of the slab than in panels (b and e) as reference. Same references as in Fig. 12 for the dashed line in panel (a). The horizontal position of the zero in panel (a) is displaced to correspond to the position of the trench (but not for the other panels). In panels (b-d) areas in red, positive values, show regions associated with extension while areas in blue, negative values, show compression. In panels (b-g) white or black lines correspond to the thermally controlled LAB (1'440°C isotherm).

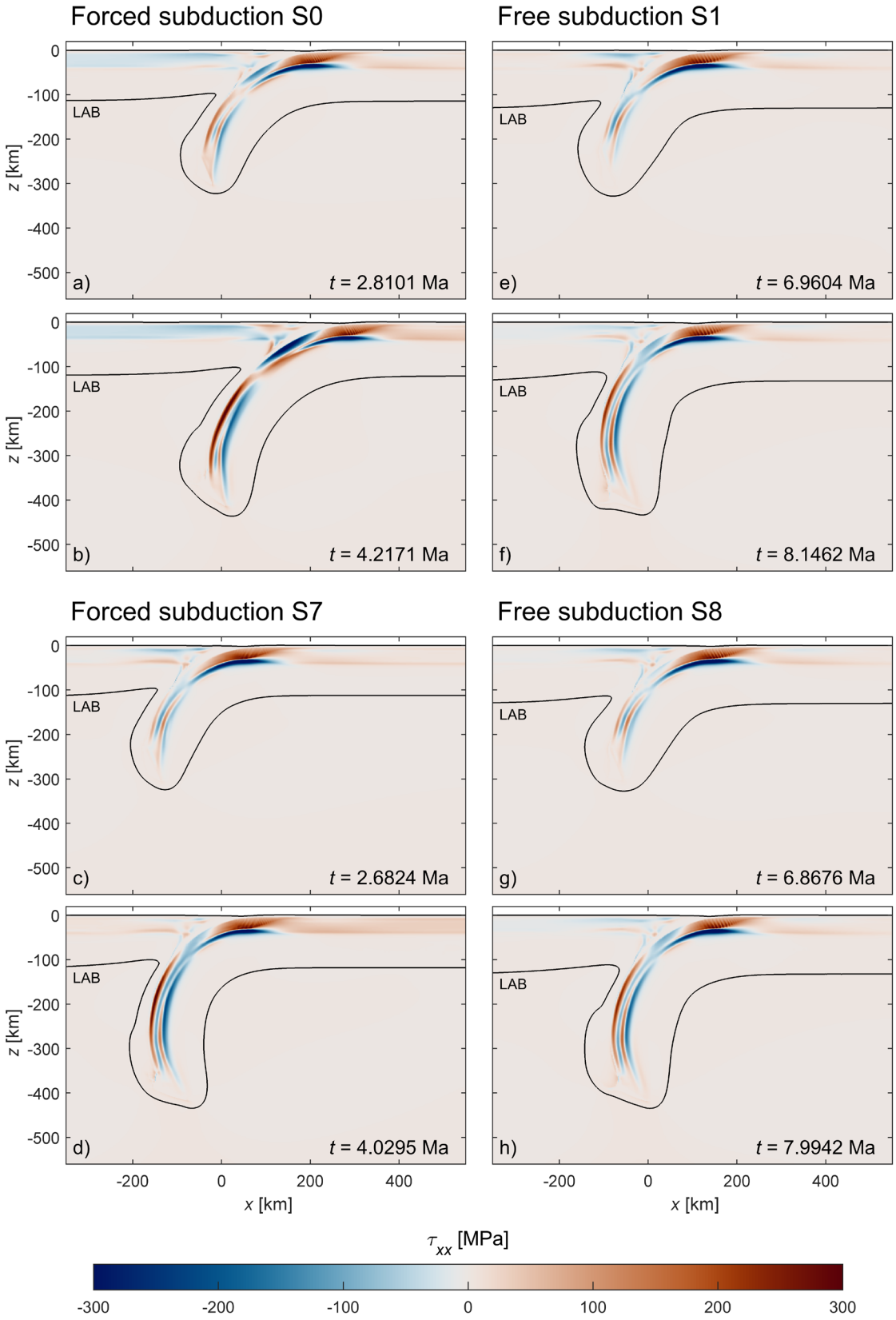

Figure 14. Colour plot of horizontal deviatoric stress for forced and free subduction with different boundary conditions.

Panels (a) and (b) show results of forced simulation S0 corresponding to the model where horizontal boundary velocities are

applied on both sides of the model. Panels (c) and (d) show results of the same forced simulation, except that a horizontal boundary velocity is only applied on the right side of the model (simulation S7, Table 2). This velocity is twice as large as the one of model S0 to maintain the same absolute convergence velocity. Panels (e) and (f) show results of free simulation S1 corresponding to the model where the lateral detachment of the slab by a weak zone is implemented at the right side of the model. Panels (g) and (h) show results of a free simulation where this detachment is applied at both sides of the model (S8). Time step for panels (a), (b), (e) and (f) same as Figs 3b, c, e and f. Time step for panels (c), (d), (g) and (h) are chosen to have the same corresponding depth of the slab (310 km and 425 km) for comparison. The areas in red, positive values, show regions associated with extension while areas in blue, negative values, show compression. Black lines correspond to the thermally controlled LAB (1'440°C isotherm).

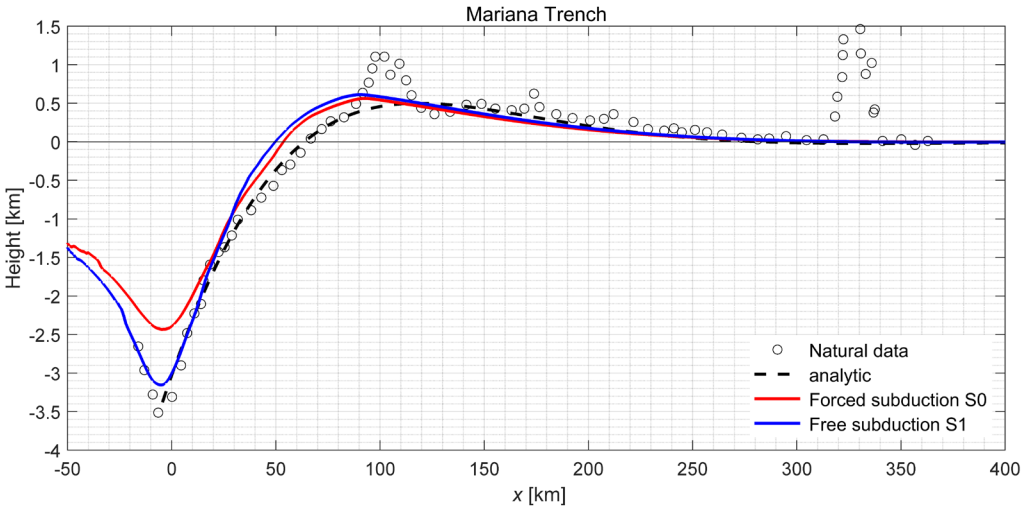

Figure 15. Comparison of the topography of the Mariana trench with modelled topography for the forced (S0) and free (S1) subduction models. The dashed line shows the best fit of elastic flexure from Turcotte & Schubert (2014) (Fig. 3.35 and equation 3.159, x_b = 55 km and w_b = 0.5 km). For comparison all topography profiles are co-located at the trench.

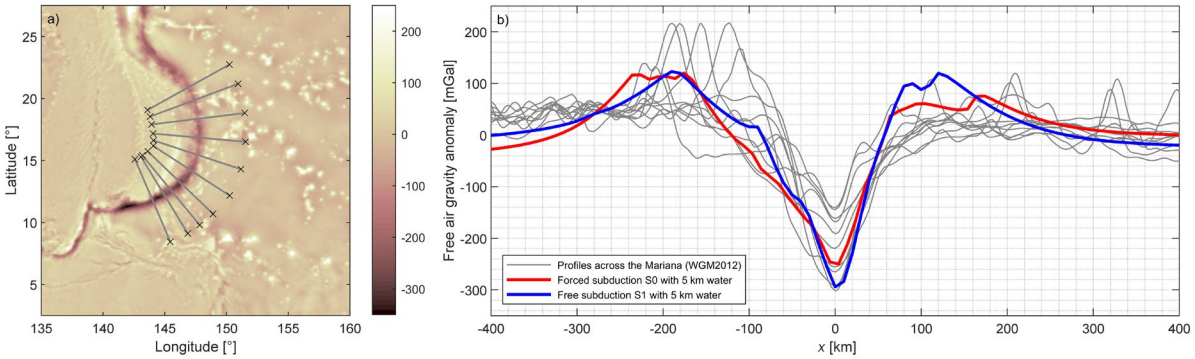

Figure 16. Free-air gravity anomaly comparison. Panel (a) shows the location of 10 different profiles across the Mariana Trench, with the WGM2012 free-air anomaly map in the background. Panel (b) shows in grey the observed profiles across the Mariana Trench, in red the synthetic profile from the forced subduction model for the time step corresponding to Fig. 3c, and in blue the synthetic profile from the free subduction model for the time step corresponding to Fig. 3f. A zoom on the trench was chosen for the horizontal position and all profiles were centred on the trench.

Table 1. Parameters used in the numerical simulations for the plastic and viscous rheology, namely dislocation creep, diffusion creep and Peierls creep. Parameters used for dry dislocation and dry diffusion mechanisms are from Hirth & Kohlstedt (2003). Parameters used for Peierls creep are from Kameyama et al. (1999).

Adopted values of rheological and physical parameters					
Viscous rheology		Lithosphere, Asthenosphere and Weak zone and weak hydrated crust			
		Dislocation	Diffusion	Peierls	Units
F	invariant formulation correction factor	$1/6 \cdot 2^{(1/n) \cdot 3(n-1/2n)}$	$1/6 \cdot 2^{(1/n) \cdot 3(n-1/2n)}$	$1/6 \cdot 2^{(1/S) \cdot 3(S-1/2S)}$	-
A	pre-exponential constant	$1.1 \cdot 10^{-16}$	$1.5 \cdot 10^{-15}$	$5.7 \cdot 10^{11}$	$[s^{-1} \cdot Pa^{-n} \cdot m^{m}]$
n	stress exponent	3.5	1	2	-
m	grain size exponent	0	3	-	-
E	activation energy	$530 \cdot 10^{3}$	$375 \cdot 10^{3}$	$5.4 \cdot 10^{5}$	$[J \cdot mol^{-1}]$
V	activation volume	$11 \cdot 10^{-6}$	$4 \cdot 10^{-6}$	0	$[m^{3} \cdot mol^{-1}]$
γ	adjustable constant	-	-	0.1	-
σ_{pei}	the Peierls stress	-	-	8.5×10^{9}	[Pa]
Plastic rheology		Lithosphere	Asthenosphere	Weak zone / Sediments	
C	cohesion	$1 \cdot 10^{7}$	$1 \cdot 10^{6}$	$1 \cdot 10^{6}$	[Pa]
Θ	Angle of internal friction	30	5	0	[°]
Constants					
R	universal gas constant	8.31			$[J \cdot mol^{-1} \cdot K^{-1}]$
α	thermal expansion	$8 \cdot 10^{-6}$			$[K^{-1}]$
β	compressibility	$1 \cdot 10^{-11}$			$[Pa^{-1}]$
d	grain size	$5 \cdot 10^{-3}$			[m]
H_R	radiogenic heat production	$1 \cdot 10^{-10}$			$[W \cdot m^{-3}]$
G	shear modulus	$3 \cdot 10^{10}$			[Pa]
g	gravity	9.81			$[m \cdot s^{-2}]$

1073 *Table 2. The main model differences of the nine simulations performed for this study.*

1074

	Parameters					
Simulations	type	t_{free}	elasticity	friction angle lithosphere	Boundary velocity	Boundary weak zone
S0 (Ref)	forced	-	yes, $G = 3 \cdot 10^{10}$ Pa	30°	both sides	none
S1	free	1.25 Ma	yes, $G = 3 \cdot 10^{10}$ Pa	30°	none	right side
S2	free	1.17 Ma	yes, $G = 3 \cdot 10^{10}$ Pa	30°	none	right side
S3	forced	-	yes, $G = 3 \cdot 10^{12}$ Pa	30°	both sides	none
S4	forced	-	yes, $G = 3 \cdot 10^{13}$ Pa	30°	both sides	none
S5	forced	-	yes, $G = 3 \cdot 10^{10}$ Pa	5°	both sides	none
S6	forced	-	yes, $G = 3 \cdot 10^{10}$ Pa	1°	both sides	none
S7	forced	-	yes, $G = 3 \cdot 10^{10}$ Pa	30°	right side	none
S8	free	1.25 Ma	yes, $G = 3 \cdot 10^{10}$ Pa	30°	none	left and right side

1075